A reversible shearing DNA probe for visualizing mechanically strong receptors in living cells

Hongyun Li[1], Chen Zhang[2], Yuru Hu[1], Pengxiang Liu[1], Feng Sun[1], Wei Chen[1], Xinghua Zhang [1,2], Jie Ma[3], Wenxu Wang[1], Liang Wang[1], Piyu Wu[1] and Zheng Liu [1✉]

In the last decade, DNA-based tension sensors have made significant contributions to the study of the importance of mechanical forces in many biological systems. Albeit successful, one shortcoming of these techniques is their inability to reversibly measure receptor forces in a higher regime (that is, >20 pN), which limits our understanding of the molecular details of mechanochemical transduction in living cells. Here, we developed a reversible shearing DNA-based tension probe (RSDTP) for probing molecular piconewton-scale forces between 4 and 60 pN transmitted by cells. Using these probes, we can easily distinguish the differences in force-bearing integrins without perturbing adhesion biology and reveal that a strong force-bearing integrin cluster can serve as a 'mechanical pivot' to maintain focal adhesion architecture and facilitate its maturation. The benefits of the RSDTP include a high dynamic range, reversibility and single-molecule sensitivity, all of which will facilitate a better understanding of the molecular mechanisms of mechanobiology.

Cells are highly dynamic in tissues, and their functions are constantly regulated by various forms of mechanical forces generated by the pushing, pulling and squeezing by both other cells and the extracellular matrix (ECM)[1–3]. The mechanical forces generated by cells in tissues are substantial and can be easily in the range of many nanonewtons. Conversely, the force per receptor is tiny, with its magnitude distributing from a few piconewtons to tens of piconewtons[4,5], but these molecular forces can precisely regulate the signal transduction process in time and space, thereby directly or indirectly controlling a number of biological responses such as cell differentiation, gene expression and apoptosis[2,6]. Cells detect the stiffness of the ECM by applying dynamic forces through integrin receptors, which ultimately transmit mechanical information as chemical cues[7,8]. Accordingly, there is a dynamic interplay between chemical and mechanical signals at the cell–ECM interface, and many details of this mechanotransduction process remain difficult to elucidate[1,9,10]. Therefore, characterizing the interaction between mechanical and biochemical signals at the molecular level is an essential part of understanding the mechanism of cellular mechanical signalling[4,6].

Over the last decade, various types of immobilized molecular fluorescent tension probes have been developed to quantitatively measure the mechanical force exerted by specific membrane proteins with piconewton sensitivity in living cells[4–6,11–13]. For example, a molecular tension fluorescence microscopy (MTFM) probe invented by Salaita and co-workers[14] is a typical reversible immobilized tension sensor that enables real-time visualization of the mechanical signals transmitted between specific cell membrane receptors and the ECM. Besides this, different variants that use polyethylene glycol (PEG)[15,16], nucleic acids[17–19] or engineered polypeptides[11,12,20] as a molecule spring with a range of 1–21 pN have been reported in the past few years, and these probes demonstrate a great advantage in the study of mechanochemical signalling interactions in living cells[4]. However, the mechanical ranges of these reversible tension sensors are not always sufficient to cover the forces transduced on membrane receptors[21]. Although the clamped

I27 protein sensor developed by Galior et al.[22] can be used to test the upper limit of integrin forces (up to 100 pN), the clamped protein sensor fails to detect strong receptor forces in living cells in real time given that dithiothreitol irreversibly breaks disulfide bonds. Recently, Wang and Ha[23–25] developed another type of DNA-based force sensor, called the tension gauge tether (TGT), which relies on the irreversible force-dependent rupture of DNA duplexes to control and measure cell adhesion forces. The rupture forces of the TGT probe can be fine-tuned by changing the position of its mechanical loading site, thereby covering a wide range of tension (12–60 pN)[26]. Nevertheless, irreversible force-induced rupture of TGT and surface ligand depletion most probably perturb the cell biology of adhesions.

Here, we overcome these challenges and develop a class of reversible shearing DNA-based tension probes (RSDTPs) by combining the concepts of TGT[23] and DNA hairpin-based tension probes[17,18]. The RSDTPs presented here are non-rupturable, digital and capable of measuring the magnitude of molecular forces from 4 to 60 pN in living cells. Furthermore, we generated a photocleavable RSDTP that allows it to switch from a reversible to an irreversible state (TGT-like probe) by light and thus enables us to examine functions of a force-bearing receptor during mechanotransduction. The unique advantages of the reversible shearing DNA probes will help us elucidate the role of mechanics in receptor function during cell adhesion and migration processes.

Results

Design and calibration of the reversible shearing DNA tension probes. The conventional DNA hairpin used to build molecular tension probes has limited tunability in mechanical stability as its force tolerance exhibits a diminishing return when the stem size is increased beyond ~20 bp, and the unzipping geometry is fixed[17,18,27]. We solved this problem by designing a new type of hairpin structure in which the rupture force can be adjusted by either varying the GC content in the unzipping geometry, as in the conventional hairpin structure, or tuning the positions of the mechanical loading sites in
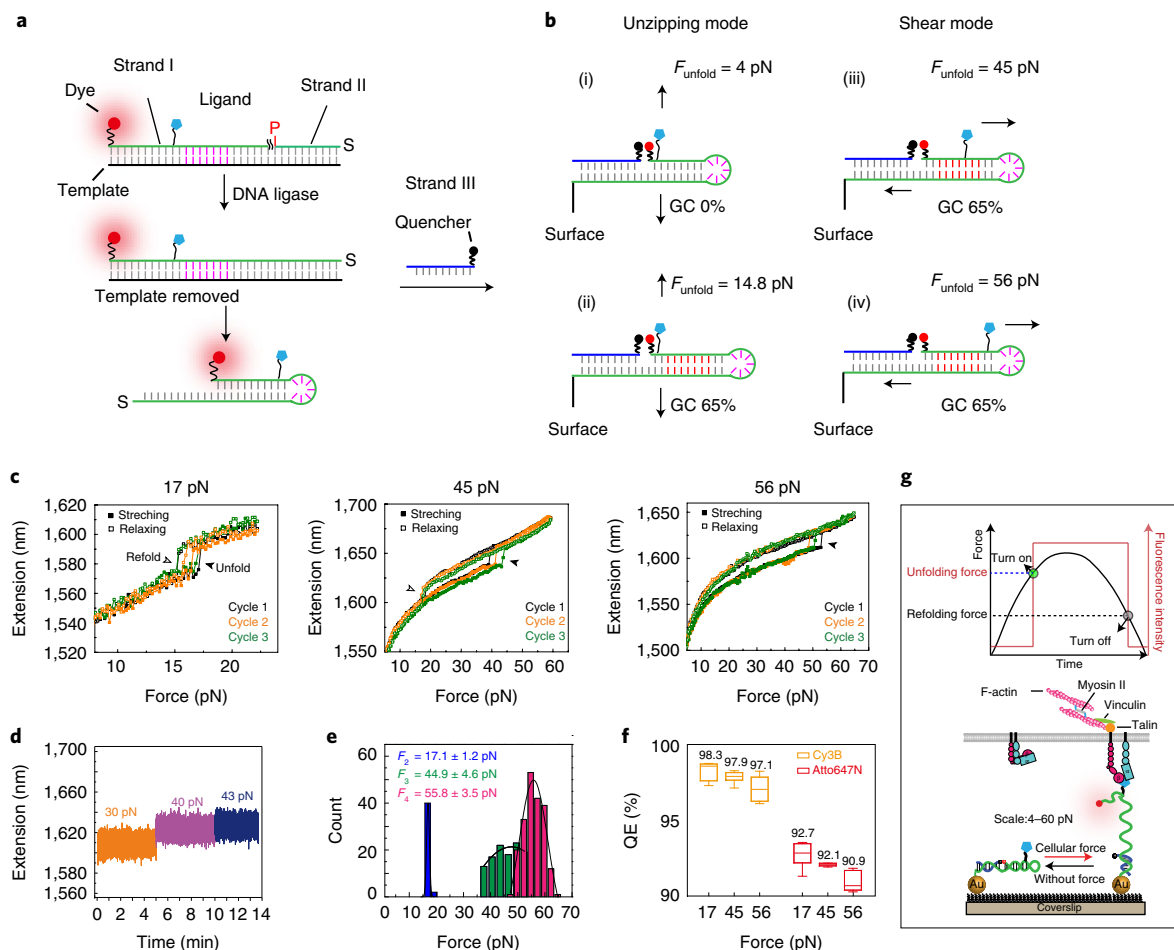
Fig. 1 | Design and characterization of the RSDTPs. a,b, Schematics of the synthesis procedures (**a**) and force-application geometries (**b**) of the RSDTPs. In **b**, (i)–(iv) illustrate that the rupture forces of the RSDTPs depend on their nucleotide sequences and force-application geometries. **c,** Calibration curves of reversible shearing DNA probes with SMMTs. Representative force-extension curves of reversible probes with three different rupture forces (17 pN, 45 pN and 56 pN) were acquired at a loading rate of 1 pN s^{-1}. Each DNA probe undergoes at least three mechanical unfolding and refolding (filled and open rectangles, respectively) cycles during the calibration. **d,** Mechanical stability testing results of 56-pN reversible shearing DNA probes. The probe does not unfold even if low-level forces (30–43 pN) are continuously applied for more than 10 min. **e,** Histograms and Gaussian-fitting results of applied forces at the unfolding events for F_2 (blue, $n = 45$), F_3 (green, $n = 102$) and F_4 (red, $n = 201$) DNA probes. **f,** QE analysis of different RSDTPs. The box represents 25th and 75th percentiles, the median is denoted by the middle horizontal line, the mean values are marked above each box, and the whiskers represent 1.5-fold the interquartile range. $n = 6$ independent experiments except the 17-pN Cy3B probe, which was four times. **g,** Upper: diagram of the response of the RSDTP to applied force. The RSDTP digitally 'turns on' when the integrin force increases above the unfolding force and 'turns off' once the integrin force drops below the refolding force. Lower: schematic of the RSDTP for mapping the integrin-mediated tension, displaying a reversible 'turn off–on' fluorescence response with cellular forces.

a shearing geometry, as in the TGT[23]. Therefore, the force required to unfold the hairpin will be determined by the ligand location and the free energy of the structure.

To assemble the RSDTPs, we first synthesized two oligonucleotide 'bricks' (strand I and II), whereby strand I consists of a Cy3B dye at the 5′-end and a cyclic RGD peptide (cRGDfK) at an internal position and strand II presents a phosphoric acid at the 5′-terminal and a thiol group at the 3′-end. Template-directed ligation generated an extra-long single-stranded DNA (elssDNA) that can form a partial hairpin structure with an overhang. Then, we hybridized the elssDNA with strand III, which binds to the overhang region of the elssDNA. The resulting DNA nanostructure was subsequently immobilized on a surface to enable real-time mapping of integrin forces in living cells (Fig. 1a,b and Extended Data Fig. 1). The force-response thresholds of the RSDTP can be easily tuned in a broad dynamic range from 4 to 60 pN by varying both the GC content and the force application geometry of the DNA hairpin, as

shown in Fig. 1b. Importantly, all the unfolding forces of the RSDTP can be mathematically predicted[23,27–29].

We synthesized a small library of RSDTPs with predicted F_{unfold} values of ~14.8, ~45.2 and ~56.8 pN (Extended Data Fig. 1 and Supplementary Tables 1 and 2). To calibrate these probes, we employed a single-molecule magnetic tweezer (SMMT) technique to examine their force-induced extension behaviours using a force ramp[30] with a constant loading rate of 1 pN s^{-1} (Fig. 1c–e and Extended Data Fig. 2). The abrupt extension in the extension-force curve (EFC) represents the hairpin unfolding event at F_{unfold}, the most probable unfolding force of the DNA probes. Although the refolding event of the 56-pN probe is difficult to be observed here due to the short transition distance, the cycle-stretching results demonstrated that all the probes could completely refold into their original conformation when the forces subsided (Fig. 1c), and the statistical F_{unfold} values of the designed reversible shearing DNA structures were 17 ± 1.2 pN, 45 ± 4.6 pN and 56 ± 3.5 pN

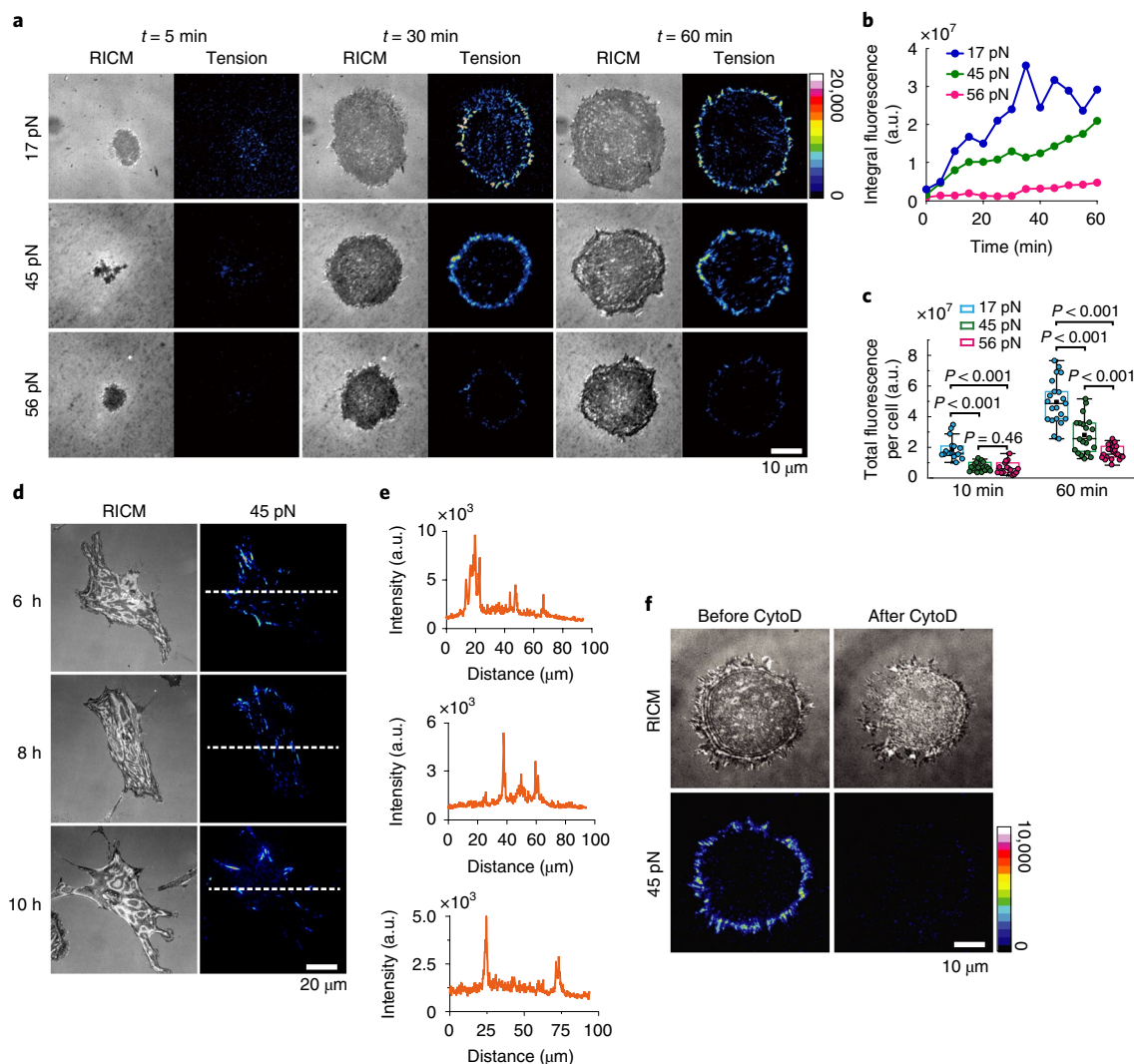**Fig. 2 | Revealing the magnitude and spatial dynamics of integrin forces in living cells with RSDTPs. a**, Representative time-lapse images of RICM and tension during spreading of NIH-3T3 cells on glass surfaces functionalized by RSDTPs with different rupture forces. Key is in arbitrary units. The images are representative of two independent biological replicates. **b**, Plots of integral tension signal intensities obtained by different RSDTPs as a function of time for NIH-3T3 cells shown in **a**. a.u., arbitrary units. **c**, Total tension signal intensities measured using different RSDTPs at two time points (10 min and 60 min). Each data point represents a single NIH-3T3 cell (*n*, number of cells: for 10 min, blue = 16, green = 18, red = 15; for 60 min, blue = 21, green = 20, red = 21). The box represents 25th and 75th percentiles, the median is denoted by the middle horizontal line, the mean is indicated by a small solid rectangle and the whiskers represent 1.5-fold the interquartile range. Two-tailed, Student's *t*-test was used to measure statistical significance, and *P* values are shown on the graph. **d**, Tension maps of living cells obtained at 6, 8 and 10 h after cell seeding on 45-pN RSDTPs. The images are representative of three independent biological replicates. **e**, Intensity profiles of the regions highlighted with dashed white lines in **d**. **f**, Representative images of RICM and integrin-mediated tension of a cell before and after treated with cytochalasin D (CytoD; 20 μM). Key is in arbitrary units. The images are representative of three independent biological replicates.

(Fig. 1e). These experimental values agreed well with the theoretical prediction (Supplementary Table 1 and Supplementary Note 1). Note that the equilibrium force of unfolding is the same for all the probes reported here because the shearing and unzipping modes have a similar likelihood of refolding as the force is reduced. This causes a significant hysteresis between unfolding and refolding forces in force spectroscopy measurements for shearing-mode probes (Fig. 1c). Therefore, the initial unfolding of the reversible shearing-mode probe should be described as an activated process, whereby the probe will separate in a time-dependent manner that also depends on the duplex length and its geometry as well as the force applied. After activation of the probe, only a low level of force is needed to maintain the probes in the open state. Accordingly, the

F_{unfold} value reported by the RSDTP represents a minimum force threshold required for the rapid activation of the probe (same as the TGT) rather than a transient force value. In addition, although the shear-induced rupture of DNA duplexes strongly depends on the time scale of observation[29], we did not observe the unfolding of the 56-pN reversible DNA probe while a low-level force (30–44 pN) was continuously applied on it for more than 10 min in our magnetic tweezer measurement (Fig. 1d and Extended Data Fig. 2). This result demonstrates that the 56-pN reversible shearing probe is mechanically stable and highly reliable for probing mechanically strong receptors in living cells.

Subsequently, the RSDTPs were modified on a gold nanoparticle (Au NP) of 5 nm in diameter (Extended Data Figs. 3 and 4), which
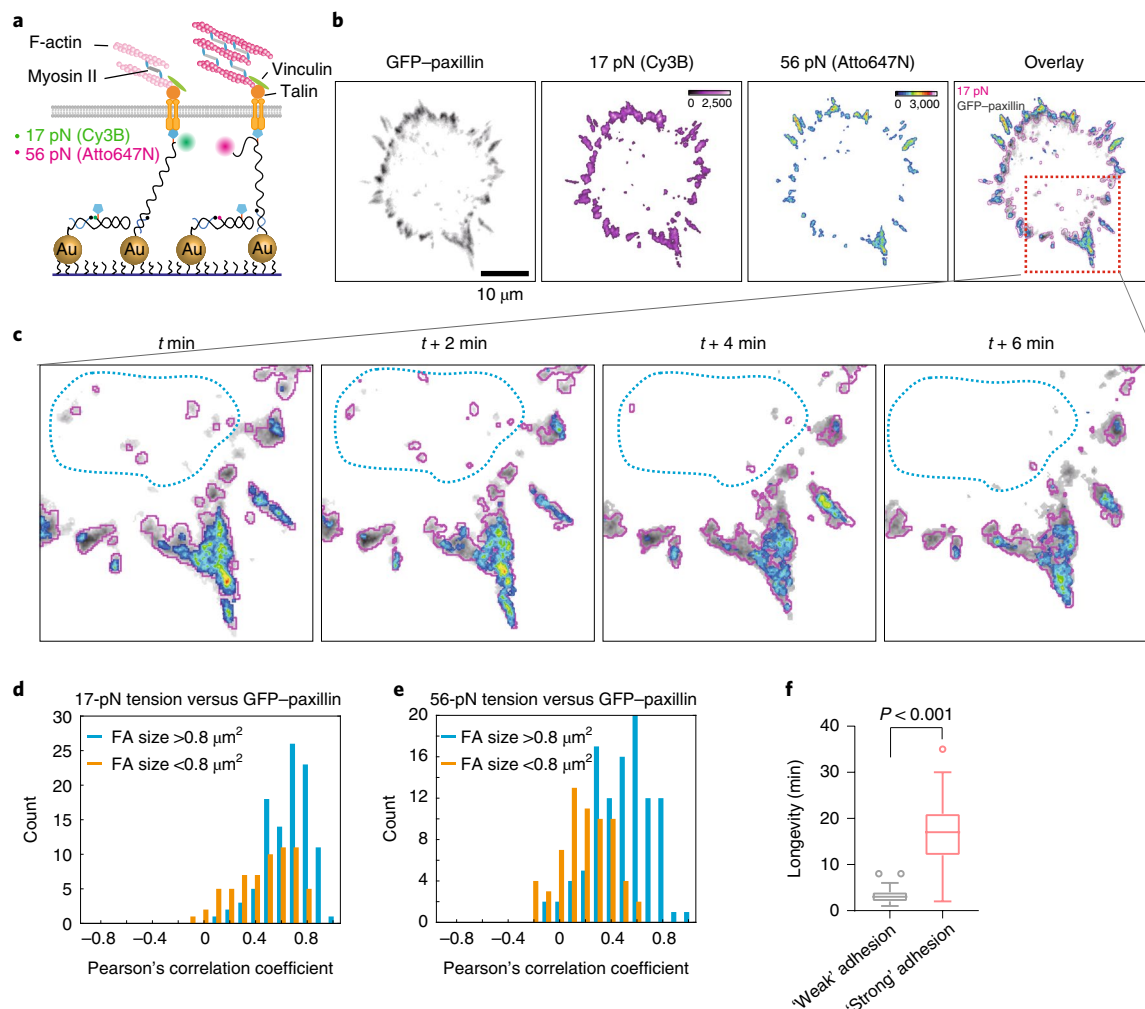
Fig. 3 | Imaging of different levels of integrin force in real time with multiplexed RSDTPs. a, Schematic of real-time force images with multiplexed RSDTPs. 17-pN (Cy3B) and 56-pN (Atto647N) RSDTPs were mixed in a 1:1 molar ratio before incubation on the coverslips. **b**, Representative TIRF images of GFP–paxillin, tension signals of 17 pN (Cy3B) and 56 pN (Atto647N) and overlay of all channels. Note that there are very few adhesions in the overlay images and that the 56-pN signal is not accompanied by the 17-pN signal, which is probably caused by photobleaching. Keys are in arbitrary units. The images are representative of three independent biological replicates. **c**, Zoom-in of the region of interest in **b** (indicated by a red rectangle) showing the dynamics of 'weak' (highlighted by blue dotted area) and 'strong' adhesion structures. **d,e**, Colocalization analysis of GFP–paxillin/17-pN signal (**d**) and GFP–paxillin/56-pN signal (**e**) using Pearson's correlation coefficient analysis ($n = 168$ FAs for each figure). **f**, Longevity of 'weak' adhesions (without 56-pN signal, $n = 88$) and 'strong' adhesions (with 56-pN signal, $n = 71$). The box represents 25th and 75th percentiles, the median is denoted by the middle horizontal line and the whiskers represent 1.5-fold the interquartile range. Statistical significance was determined using a two-tailed Student's t-test, and P values are shown on the graph.

was immobilized on a substrate following a method reported by the Salaita Lab[15,31,32]. When the DNA hairpin is in a folded state, its fluorophore is highly quenched by a black hole quencher (BHQ) and the Au NP through both fluorescence resonance energy transfer and nanometal surface energy transfer (NSET) pathways, thereby boosting the sensitivity of the tension probes. The quenching efficiency (QE) measurements showed that labelling the probes with either a Cy3B or an Atto647N fluorophore yielded good QE values (Fig. 1f, Extended Data Fig. 5 and Supplementary Note 2). No significant differences in QE measurements were observed for different ranges of probe, which indicates that the NSET effect of the 5-nm Au NP is negligible for all mechanically unfolded reversible DNA probes. Therefore, once the cell applies a dynamic force to a substrate through the RGD ligand on the probes, the RSDTPs can reversibly indicate whether the cellular force transmitted on each integrin–RGD bond has reached a defined threshold (Fig. 1g).

RSDTPs reveal the heterogeneity of integrin tension in real time. To demonstrate that RSDTPs can detect different ranges of integrin tension in real time, we plated NIH-3T3 cells onto a series of substrates modified with the above-mentioned probes to mimic the mechanical interaction between fibroblasts and the ECM. Then, we recorded time-lapse videos capturing the initial adhesion and spreading of these cells and the dynamics of the integrin tension signals using reflection interference contrast microscopy (RICM) and total internal reflection fluorescence (TIRF) microscopy, respectively. Cells seeded on the 17-pN RSDTP generated a tension signal that was diffuse and appeared in puncta of higher intensity within minutes (Fig. 2a, 5 min). After 1 h, the majority of the tension signal was localized at the cell edge and exhibited a long rod-like contact pattern resembling focal adhesions (FAs) (Fig. 2a, 60 min). These results are consistent with previous observations using MTFM probes[15,17,18], thereby demonstrating the reliability of the RSDTP

in mapping cell traction forces. Cells seeded on the 56-pN RSDTP also generated an integrin force sufficient enough to unfold the probes with similar tension patterns, albeit the fluorescence intensities were significantly lower. This indicates that a small number of mechanically strong integrin clusters (>56 pN; 'mechanical hotspots') existed in the FAs (Fig. 2b,c and Supplementary Video 1).

In addition, high-quality tension images could be observed for at least 10 h by exchanging the imaging medium every 2 h (Fig. 2d,e). The tension signals disappeared immediately when we treated cells with cytochalasin D to eliminate the cytoskeleton (Fig. 2f and Extended Data Fig. 6). Taken together, these results demonstrate that the RSDTPs are reversible and highly stable on the surface, allowing us to determine whether a molecular force had reached a defined threshold in real time. More importantly, these results show that RSDTPs combine the technical advantages of the TGT probe and conventional DNA hairpin-based tension sensors, thus enabling us to reversibly and digitally measure a wide range of forces (4–60 pN) in living cells.

Imaging the dynamics of different levels of force with multiplexed RSDTPs. To further investigate the dynamic features of the mechanical hotspots during cell adhesion processes, we cultured NIH-3T3 cells expressing green fluorescent protein (GFP)–paxillin on a multiplexed RSDTP surface, which consisted of 17-pN (Cy3B) and 56-pN (Atto647N) RSDTPs, and simultaneously recorded the dynamics of GFP–paxillin, 17-pN and 56-pN tension during early cell adhesion and spreading (Fig. 3, Extended Data Fig. 7 and Supplementary Fig. 1). After 5 min of cell spreading, we observed significant integrin tension above 17 pN and 56 pN, and the tension patterns in both channels exhibited high similarity. The integrin tension >17 pN existed in puncta and elongated structures, while integrin tension >56 pN mainly formed rod-like structures with diameters smaller than that reported by the 17-pN RSDTP (Fig. 3b,c). Correlation analysis between the tension map and GFP–paxillin of each adhesion demonstrated that the 56-pN signal was moderately colocalized with GFP–paxillin only in larger adhesion structures (>0.8 μm² in size) while the 17-pN signal was nearly perfectly colocalized with GFP–paxillin sites (Fig. 3d,e). In addition, 17-pN and 56-pN overlaying images suggested that a force gradient existed in the more mature FAs, and the hotspots were surrounded by weak force integrins, which is consistent with recent reports using a differential TGT analysis method[30]. Interestingly, two-colour time-lapse imaging revealed that FAs carrying less strong integrins appeared to rapidly dissociate and exhibit short longevity (1–3 mins). In contrast, the FAs carrying more strong integrins were more likely to grow into elongated mature FAs and had an average longevity of up to 17 min (Fig. 3f). Although integrins with forces weaker than 17 pN in adhesions are not visualized

here, these observations demonstrate that the nascent adhesions bear a low level of force and that strong integrins are tightly correlated with long-lived adhesion structures. Taken together, these observations demonstrate that the multiplexed RSDTPs allowed us to clearly distinguish and track the dynamics of the different magnitudes of integrin forces in living cells.

**Mechanically strong integrins maintain the FA architecture.** To further examine the function of the mechanically strong integrins for FA architecture, we first limited the integrin force transmission of >56 pN by using 56-pN non-fluorescent TGT probes. This will restrict the accumulation of strong integrin receptors at the FAs because these receptors will irreversibly rupture the 56-pN TGT probes and cease the integrin mechanical signalling process (Fig. 4a). We found that adhesions labelled with GFP–paxillin of the NIH-3T3 cells seeded on the 100% 56-pN TGT-probe-coated surface were notably more dynamic compared with cells seeded on the 100% 56-pN RSDTP-coated and fibronectin-coated surface (Fig. 4b and Supplementary Video 2). To illustrate the differences in FA dynamics of cell spreading on the 56-pN irreversible and 56-pN reversible DNA probe substrates, FAs were colour-coded on the basis of their presence at different time points in the time-lapse videos using FA analysis software[33] (Fig. 4b). We observed a high-density trace of FAs at the cell perimeter when the cells were cultured on the 100% 56-pN TGT surfaces, while the FAs of cells seeded on the 100% 56-pN RSDTP or fibronectin-coated surface appeared in smaller diameters. Statistical analysis of the FA dynamics showed that the FAs with strong integrins had longer longevity and larger size (Fig. 4c,d). To rule out the contribution of 56-pN TGT ligand depletion to adhesion dynamics, we mixed approximately 2% of the 56-pN RSDTP into 56-pN TGT probe solution, and this mixture was then coated onto a surface (Fig. 4a). We tracked the dynamics of cell adhesion on this mixed-probe surface, which should have a similar ligand-depletion rate as a 100% 56-pN TGT-coated surface. Interestingly, the maximum size and the longevity of FAs of the cell spread on the mixed-probe surface were close to the 100% 56-pN reversible DNA probe (Fig. 4c,d and Supplementary Video 2). These results demonstrate that mechanically strong integrins contribute to the maintenance of the FA architecture.

We next attempted to interrupt the linkage of these strong integrins to the ECM on this mixed surface to determine how FAs respond to the mechanical balance perturbation events. To achieve this goal, we designed a photocleavable RSDTP by attaching a photocleavable group to the loop of the 56-pN probe (Fig. 4e,f). Unlike the recently developed releasable photocleavable-hairpin probes[34], the photocleavable RSDTP enables it to switch from a reversible to an irreversible state (TGT-like structure) via 365-nm ultraviolet (UV) light, which enables us to specifically cleave the strong

Fig. 4 | Mechanically strong integrins maintain the FA architecture. a, Schematic showing different FA stabilities of cells adhering to TGTs, RSDTPs and mixed probes (TGTs doped with 2% RSDTPs). High integrin forces were inhibited due to the rupture of doubles-stranded DNA (dsDNA) while cells engaged to 56-pN TGTs, but remained both on RSDTPs and mixed-probe surfaces. **b**, RICM (left) and GFP–paxillin images (middle) of a NIH-3T3 cells engaged to 56-pN non-fluorescent TGTs, 56-pN RSDTPs and mixed probes. Right: the entire set of FAs from 61 time-lapse frames over 60 min overlay the adhesions from each frame using a different colour for the set of adhesions at each time point. The images are representative of three independent experiments. **c,d**, Averages of longevity (**c**) and the maximum reachable area (**d**) of FAs when cells spread on different surfaces. Data represent the mean ± s.d.; TGT = 9 cells, RSDTP = 5 cells, mixed probes = 3 cells and fibronectin (FN) = 6 cells. Each point represents the mean value of all FAs in a single cell. Unpaired two-tailed Student's *t*-test was used to determine statistical significance, and *P* values are shown on the graph. NS, not significant. **e**, Schematic of photocleavable RSDTP. A photocleavable linker and a non-nucleotide moiety were incorporated into the sugar-phosphate backbone within the loop region, linking two nucleotide sequences through a short, UV-photocleavable C3 spacer arm. **f**, Denaturing polyacrylamide gel electrophoresis image showing the photocleaving efficiency under different UV exposure times. The experiment was repeated once. **g**, Upper: schematic of the periodic pulse of UV 365-nm illumination (0.25 Hz frequency, 1.3×10^{-4} μW μm⁻²) used to reduce cell damage. Lower: time-lapse TIRF images of GFP–paxillin and single-molecule tension signals of a GFP–paxillin-expressing cell adhered to a mixed-sensor surface (2% 56-pN photocleavable RSDTP and 98% 56-pN TGT) show dynamic changes of FAs before and after photocleavage. The images are representative of three independent replicates. **h**, FA longevities of the cell in **g** before and after photocleavage. Data represent the mean ± s.d.; each point represents a single FA; *n* = 679 within 20 min before photocleavage and *n* = 336 within 20 min after photocleavage. Two-tailed Student's *t*-test was used to determine the statistical significance, and *P* values are shown on the graph.

integrins and simultaneously monitor the changes in adhesion dynamics (Extended Data Fig. 8). Subsequently, we also doped 2% 56-pN photocleavable RSDTPs to a 56-pN non-fluorescent TGT

probe surface and then simultaneously imaged cell morphology (via RICM), FA dynamics and strong integrins lit up by a 56-pN photocleavable RSDTP. Since there were only 2% 56-pN photocleavable
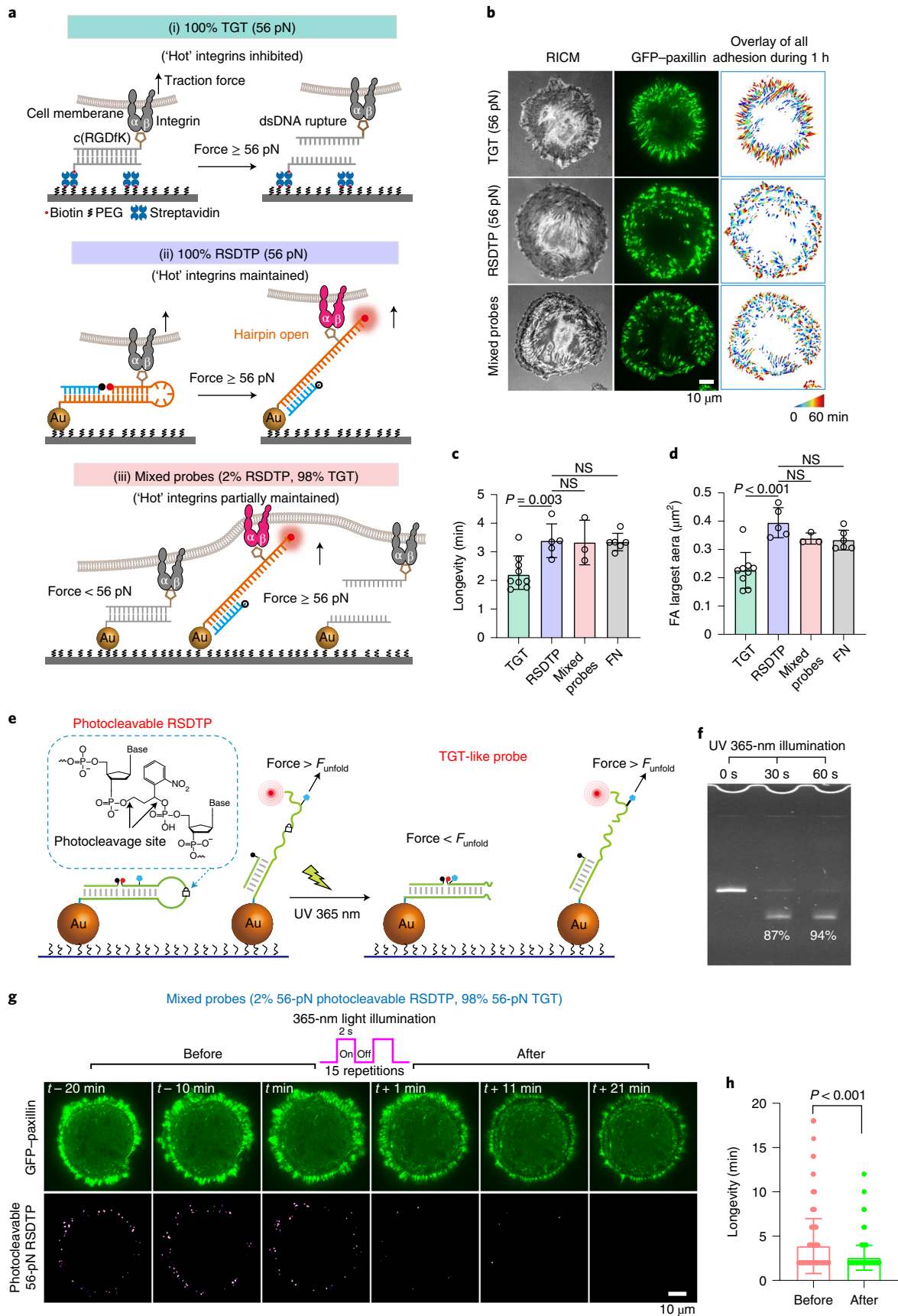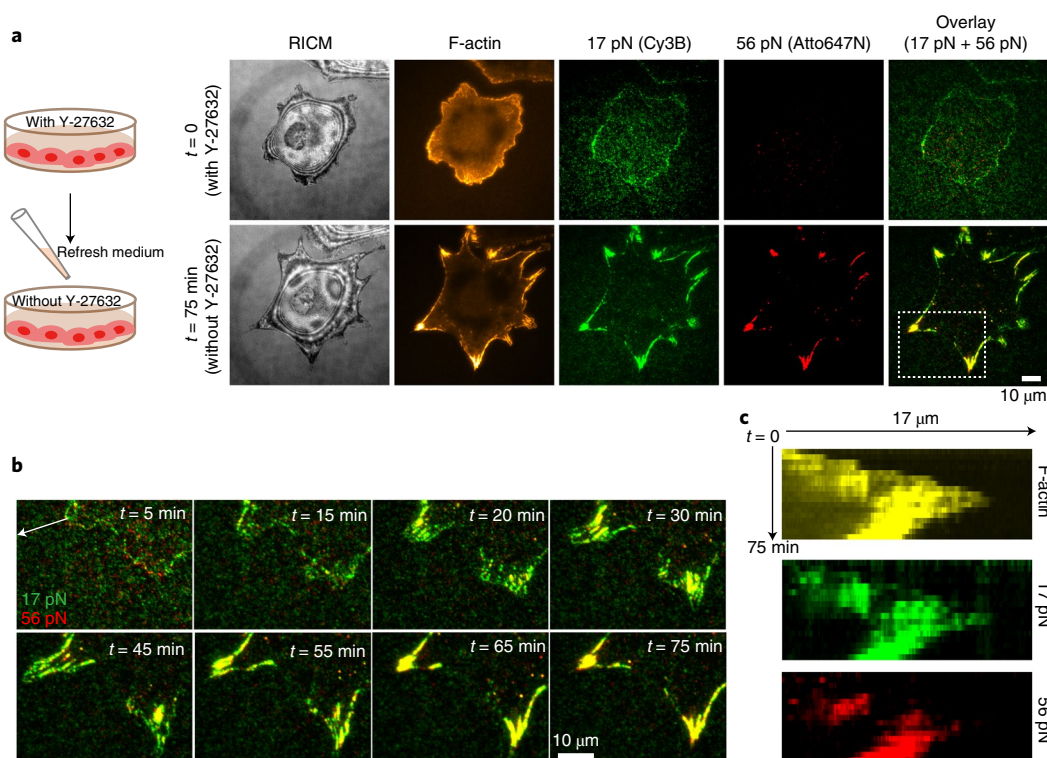
Fig. 5 | Drug treatment shows that the activity of myosin II dominates strong integrin forces. a, Left: schematic of the experimental procedures. Right: representative RICM and GFP–actin tension maps of the 17-pN probe (Cy3B, green), the 56-pN probe (Atto647N, red) and overlay of the 17-pN and 56-pN tension signals for a single NIH-3T3 cell spreading on a multiplexed RSDTP substrate before and after washing out the Y-27632 in the culture medium. Cells were pretreated with 20 μM Y-27632 before seeding on a substrate. Images in the upper row were acquired before the refresh medium, and the images in the lower row were acquired for 75 min after washing out Y-27632. **b**, Zoom-in time-lapse overlay images of integrin tensions during the recovery of myosin II activity. **c**, Kymographs (measured across the white arrow in **b**) illustrate that the F-actin contractions were correlated with increased integrin forces. The images are representative of three independent biological replicates.

RSDTPs on the surface (approximately 13 photocleavable reversible DNA probes buried in 658 irreversible TGT molecules in an area of 1 μm^2), this resulted in an extremely low opening rate of photocleavable RSDTPs during cell adhesion. Thus, 56-pN photocleavable RSDTP signals exhibited a single-molecule characteristic before cleavage (Fig. 4g and Supplementary Fig. 1d). After 365-nm light illumination for 30 s, we found that the single-molecule tension signals rapidly disappeared, which indicates that most 56-pN photocleavable RSDTPs had been photocleaved and turned into 56-pN irreversible DNA duplex structures. Remarkably, we observed that the larger FAs undergo rapid disassembly, and the newly generated FAs become more dynamic (Fig. 4g and Supplementary Video 3). Statistical analysis of the dynamics of cell adhesions showed that the longevity of the FAs was significantly reduced after photocleavage (Fig. 4h). Importantly, control experiments showed that there was no significant effect on adhesion dynamics using the same light illumination conditions on 100% 56-pN RSDTP or 100% 56-pN TGT probe surfaces (Extended Data Fig. 8b). Taken together, photocleavable RSDTPs further reveal that the stability of the FA architecture is governed by strong integrins even at the single-molecule level. Although further work is needed to fully elucidate the biochemical mechanisms underlying the unique function of strong integrins, the photocleavable RSDTPs display a unique capability to examine the mechanical function of a receptor exposed to a specific range of force during mechanotransduction.

Multiplexed RSDTPs distinguish myosin- and actin-polymerization-driven forces. Using multiplexed RSDTPs, we next investigated the contributions of actin polymerization and

myosin contractility to the magnitude of integrin forces. To eliminate myosin II activity, NIH-3T3 fibroblasts expressing GFP–actin were pretreated with the ROCK inhibitor Y-27632 (20 μM) before seeding on the multiplexed RSDTP surface, and the drug was washed away after 1 h. The results showed that the integrin tension signals after treatment with the ROCK inhibitor were exclusively localized around the thin edges of the cell (Fig. 5a). This is consistent with previous observations using a PEG-based nanoparticle tension probe[35] and suggest that the 17-pN tension signals at the leading edge of the cell were mainly driven by actin polymerization[3,36,37]. In addition, no 56-pN tension signal appeared before drug washing, which indicates that myosin contractility is the primary driver to deliver >56-pN integrin tension transmitted at the mechanical hotspots. After removing the ROCK inhibitor, 56-pN tension puncta began to appear and localize at the tips of F-actin bundles. Subsequently, actin stress fibres and FAs grew in size, and this phenomenon was accompanied by significant enhancement of the 56-pN tension signals, followed by initiation of the retraction of actin protrusions (Fig. 5b and Supplementary Video 4). This process was clearly visible in the kymograph images (Fig. 5c), which showed that the protrusion retracted along with the reinforcement of the F-actin and the increase in 56-pN tension signals. This result indicates that strong integrins not only stabilize the FA structure but are also essential for facilitating the protrusion–retraction switches of the lamellipodia in fibroblasts.

Determination of the magnitude of actin-polymerization-driven force and numbers of active integrins in a nascent adhesion. To further determine the magnitude of integrin forces driven by actin
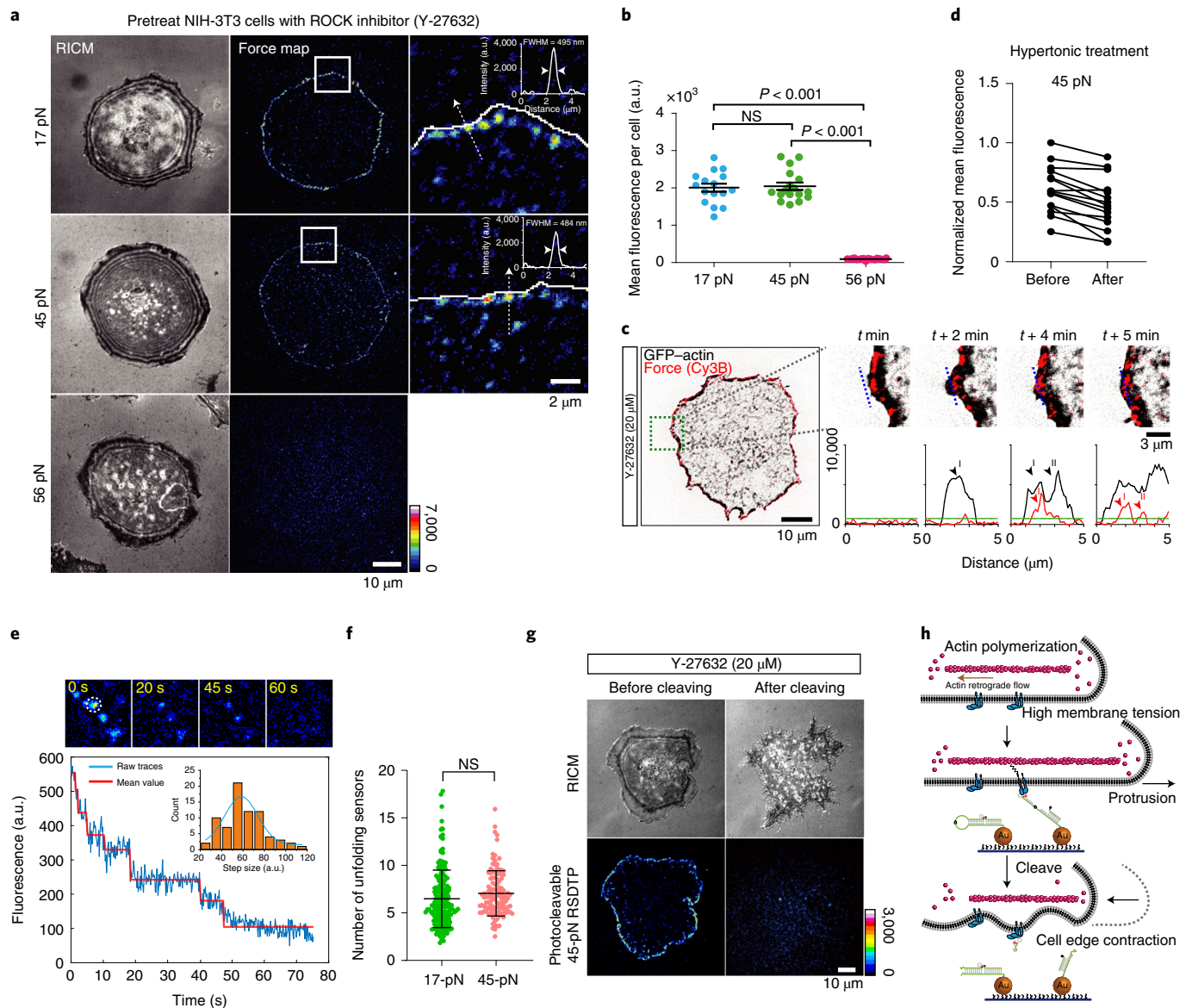
Fig. 6 | Characterization of actin-polymerization-driven integrin forces. a, RICM and molecular force images of NIH-3T3 cells adhering to RSDTPs with different rupture forces after treatment with Y-27632 selected from three independent replicates. Zoom-in (from the regions highlighted by the white squares in the middle column) images illustrate that the tension signals were arranged in clusters on the cell edge. Inset (right images), intensity profile of the white dotted line across the cell edge; the arrow marks the position of the half maxima, and the measured full width at half maxima (FWHM) is also presented. Key is in arbitrary units. **b**, Average tension signal under cells as a function of a rupture force. Data represent the mean ± s.e.m. derived from $n=16$ (17 pN), 17 (45 pN), 14 (56 pN) cells across three independent experiments. **c**, Left: overlay image of GFP–actin (black) and 45-pN tension map (red) for a Y-27632-treated cell. Right: zoomed-in time-lapse overlay images showing the generation of integrin tension following cell protrusion. Arrowheads mark the peak intensity appearing in these two fluorescence channels. Linescan analysis of the two fluorescence channels (presented for each time point) shows the arrival of the lamellipodia, followed by the increase of integrin tension. The representative cell was selected from two independent biological replicates. **d**, Average tension signal (45 pN) intensity before and after hypertonic shock. $n=15$ cells. Measurements were taken 5 min after hypertonic shock. **e,f**, Number of force-bearing integrins within each cluster. **e**, Upper: selected time-lapse images of tension signal clusters over 500 exposures of 200-ms duration for a Y-27632 pretreated fixed NIH-3T3 cell adhering to 45-pN probes. Lower: photobleaching trace of a cluster denoted by the dashed ellipse in the force map (blue, raw data; red, averages before and after each bleaching event). Inset: step size of each bleaching event (blue, Gaussian distribution curve), $n=74$ steps from two cells. **f**, Number of force-bearing integrins within each cluster was calculated by the fluorescence intensity of each tension cluster divided by average step size (in **e**). Data represent the mean ± s.d. derived from 183 (17 pN) and 118 (45 pN) clusters in each of three cells adhering to different sensor surfaces. **g**, Representative RICM and tension image of a Y-27632 pretreated cell before and after photocleavage. Key is in arbitrary units. The representative cell was chosen from two independent biological replicates. **h**, Proposed model for the force-bearing integrins forming a scaffolding that opposes the force of actin polymerization. Cutting the linkage between these force-bearing integrins and ECM using photocleavable RSDTP can cause protrusion retraction. Statistical significance was determined using two-tailed *t*-test.

polymerization, we cultured NIH-3T3 fibroblasts pretreated with Y-27632 on 17-, 45- and 56-pN RSDTP substrates. After ~40 min of cell seeding, most cells spread in an isotropic manner like a pancake on these substrates and formed a distinct lamellipodium at the periphery of cells (Fig. 6a). The cells were still capable of generating integrin forces >45 pN (but not >56 pN) at the cell

periphery that resembled nascent FAs after inhibiting the Rho kinase (Fig. 6a,b). Similar results were observed when cells were treated with blebbistatin, a myosin II ATPase inhibitor (Extended Data Fig. 9a). The puncta-like signals generated by these cells rapidly decreased to background levels after further treatment with cytochalasin D (Extended Data Fig. 9b). By transfecting NIH-3T3 cells with GFP–paxillin or GFP–actin, we found that the puncta-like tension signals colocalized with paxillin and actin at the leading edge of the cells (Fig. 6c and Extended Data Fig. 9c). Moreover, tracking the dynamics of F-actin and the puncta-like tension signals showed that the tension increased following the recruitment of F-actin (Fig. 6c and Supplementary Video 5). Taken together, these results further suggest that the puncta-like tension signals along the leading edge of cells are only generated by actin polymerization.

By quantifying the mean tension signal intensity of each cell, we found that both the 17-pN and the 45-pN RSDTPs showed an unbiased response to integrin forces driven by actin polymerization, while the signal from the 56-pN probe was close to the background level (Fig. 6a,b). Therefore, we concluded that the force exerted by the individual integrins at nascent FAs transmitted a peak force of ~45 pN, which could explain an interesting phenomenon observed using the TGT probe, whereby stable cell adhesion is possible only if the TGT probe is stronger than 40 pN and not below, and this threshold is not dependent on myosin II activity but rather requires the actin cytoskeleton[23]. In addition, we found that the intensity of these tension signals near the cell periphery dramatically decreased after osmotic changes induced by sucrose (Fig. 6d and Extended Data Fig. 9d), which provides direct evidence to support the hypothesis proposed by Wang and Ha[23] that the magnitude of the myosin-independent integrin force depends not only on actin polymerization but also on cell membrane tension. In addition, zooming in on the force maps showed that the tension signals generated by the nascent FAs from both the 17-pN and 45-pN probes were exclusively localized to a 500-nm linewidth at the cell edge and consisted of multiple individual nanocluster arrangements (Fig. 6a). To determine the number of integrins in a nanocluster that transmits forces driven by actin polymerization during the formation of protrusions, we employed the single-molecule photobleaching method[38] to count the numbers of opened RSDTPs in each integrin nanocluster. Following continuous illumination of the cell with a 561-nm laser in TIRF microscopy, approximately 30% of spots showed a clear stepwise decrease in the intensity decay curves (Fig. 6e and Extended Data Fig. 10). Using the average intensity of these photobleaching steps, we could estimate approximately an average of 7 integrin molecules in each integrin nanocluster that transmitted a peak force of ~45 pN (Fig. 6f). Furthermore, we observed a rapid retraction of the protrusion at the cell edge if the linkages between these force-bearing integrins and ECM were cut using the photocleavable RSDTP method (Fig. 6g,h), which suggests that these force-bearing integrins play a main part in each integrin cluster to counterbalance the force of actin polymerization.

Discussion

In recent years, DNA-based mechano-technology tools have been instrumental in studying the importance of mechanical forces in many biological systems[13]. However, the respective shortcomings of these techniques, such as the irreversible rupture of TGTs under force and relatively limited dynamic range of the DNA hairpin probes, limited our ability to distinguish and explore the function of mechanically distinct receptors in cellular mechanotransduction. This study established RSDTPs that can dynamically quantify molecular piconewton-scale forces in the range of 4–60 pN transmitted by cells. By implementing a design to strategically place the ligand at virtually any position of the hairpin structure, we demonstrated the tunability of the F_{unfold} of this type of force sensor, as measured using SMMT. Reversible shearing DNA probes also

benefit from the digital response of the hairpin structure[17,18], allowing quantitative interpretation of molecular forces larger than the F_{unfold} of the hairpin and therefore can be used to estimate the number of mechanically active receptors using single-molecule fluorescence measurements.

More importantly, RSDTPs can reversibly report high forces while not suffering from ligand depletion or destabilization of cell adhesion sites. Therefore, measurements with reversible shearing DNA probes do not perturb adhesion biology. Furthermore, we engineered a photocleavable RSDTP that allows it to switch from a reversible to an irreversible state by light. The unique function of the photocleavable RSDTP will enable us to examine the functions of the receptor after a specific force range during mechanotransduction. Our results showed that integrins in ascent adhesions bearing a weak force initiate FA formation, and integrins transmitting a strong force (>56 pN) act as 'mechanical pivots' to support FA maturation. Furthermore, the combination of photocleavable RSDTP and TGT probes revealed that mechanically strong integrins regulate the stability of FAs even at the single-molecule level.

Altogether, our results demonstrated the need for new biophysical tools to study molecular mechanisms of force transduction and subsequent biochemical signalling. We believe that the reversible shearing DNA probe will become a valuable toolkit for studying a wide range of mechanobiology questions pertaining to T cells[31,32,39], B cells[40] and platelets[41–43].

Online content

Any methods, additional references, Nature Research reporting summaries, source data, extended data, supplementary information, acknowledgements, peer review information; details of author contributions and competing interests; and statements of data and code availability are available at https://doi.org/10.1038/s41556-021-00691-0.

References

1. Iskratsch, T., Wolfenson, H. & Sheetz, M. P. Appreciating force and shape—the rise of mechanotransduction in cell biology. *Nat. Rev. Mol. Cell Biol.* **15**, 825–833 (2014).
2. Schwartz, M. A. The force is with us. *Science* **323**, 588–589 (2009).
3. Parsons, J. T., Horwitz, A. R. & Schwartz, M. A. Cell adhesion: integrating cytoskeletal dynamics and cellular tension. *Nat. Rev. Mol. Cell Bio.* **11**, 633–643 (2010).
4. Roca-Cusachs, P., Conte, V. & Trepat, X. Quantifying forces in cell biology. *Nat. Cell Biol.* **19**, 742–751 (2017).
5. Liu, Y., Galior, K., Ma, V. P. Y. & Salaita, K. Molecular tension probes for imaging forces at the cell surface. *Acc. Chem. Res.* **50**, 2915–2924 (2017).
6. Polacheck, W. J. & Chen, C. S. Measuring cell-generated forces: a guide to the available tools. *Nat. Methods* **13**, 415–423 (2016).
7. Kechagia, J. Z., Ivaska, J. & Roca-Cusachs, P. Integrins as biomechanical sensors of the microenvironment. *Nat. Rev. Mol. Cell Bio.* **20**, 457–473 (2019).
8. Kanchanawong, P. et al. Nanoscale architecture of integrin-based cell adhesions. *Nature* **468**, 580–584 (2010).
9. Hoffman, B. D., Grashoff, C. & Schwartz, M. A. Dynamic molecular processes mediate cellular mechanotransduction. *Nature* **475**, 316–323 (2011).
10. Plotnikov, S. V., Pasapera, A. M., Sabass, B. & Waterman, C. M. Force fluctuations within focal adhesions mediate ECM-rigidity sensing to guide directed cell migration. *Cell* **151**, 1513–1527 (2012).
11. Morimatsu, M., Mekhdjian, A. H., Adhikari, A. S. & Dunn, A. R. Molecular tension sensors report forces generated by single integrin molecules in living cells. *Nano Lett.* **13**, 3985–3989 (2013).
12. Morimatsu, M., Mekhdjian, A. H., Chang, A. C., Tan, S. J. & Dunn, A. R. Visualizing the interior architecture of focal adhesions with high-resolution traction maps. *Nano Lett.* **15**, 2220–2228 (2015).
13. Ma, V. P.-Y. & Salaita, K. DNA nanotechnology as an emerging tool to study mechanotransduction in living systems. *Small* **15**, 1900961 (2019).
14. Stabley, D. R., Jurchenko, C., Marshall, S. S. & Salaita, K. S. Visualizing mechanical tension across membrane receptors with a fluorescent sensor. *Nat. Methods* **9**, 64–67 (2011).

15. Liu, Y., Yehl, K., Narui, Y. & Salaita, K. Tension sensing nanoparticles for mechano-imaging at the living/nonliving interface. *J. Am. Chem. Soc.* **135**, 5320–5323 (2013).

16. Chang, Y. et al. A general approach for generating fluorescent probes to visualize piconewton forces at the cell surface. *J. Am. Chem. Soc.* **138**, 2901–2904 (2016).

17. Blakely, B. L. et al. A DNA-based molecular probe for optically reporting cellular traction forces. *Nat. Methods* **11**, 1229–1232 (2014).

18. Zhang, Y., Ge, C., Zhu, C. & Salaita, K. DNA-based digital tension probes reveal integrin forces during early cell adhesion. *Nat. Commun.* **5**, 5167 (2014).

19. Brockman, J. M. et al. Live-cell super-resolved PAINT imaging of piconewton cellular traction forces. *Nat. Methods* **17**, 1018–1024 (2020).

20. Tan, S. J. et al. Regulation and dynamics of force transmission at individual cell-matrix adhesion bonds. *Sci. Adv.* **6**, eaax0317 (2020).

21. Jurchenko, C., Chang, Y., Narui, Y., Zhang, Y. & Salaita, K. S. Integrin-generated forces lead to streptavidin-biotin unbinding in cellular adhesions. *Biophys. J.* **106**, 1436–1446 (2014).

22. Galior, K., Liu, Y., Yehl, K., Vivek, S. & Salaita, K. Titin-based nanoparticle tension sensors map high-magnitude integrin forces within focal adhesions. *Nano Lett.* **16**, 341–348 (2016).

23. Wang, X. & Ha, T. Defining single molecular forces required to activate integrin and notch signaling. *Science* **340**, 991–994 (2013).

24. Zhao, Y. C., Wang, Y. L., Sarkar, A. & Wang, X. F. Keratocytes generate high integrin tension at the trailing edge to mediate rear de-adhesion during rapid cell migration. *iScience* **9**, 502–512 (2018).

25. Zhao, Y. C., Pal, K., Tu, Y. & Wang, X. F. Cellular force nanoscopy with 50 nm resolution based on integrin molecular tension imaging and localization. *J. Am. Chem. Soc.* **142**, 6930–6934 (2020).

26. Jo, M. H., Cottle, W. T. & Ha, T. Real-time measurement of molecular tension during cell adhesion and migration using multiplexed differential analysis of tension gauge tethers. *ACS Biomater. Sci. Eng.* **5**, 3856–3863 (2019).

27. Woodside, M. T. et al. Nanomechanical measurements of the sequence-dependent folding landscapes of single nucleic acid hairpins. *Proc. Natl Acad. Sci. USA* **103**, 6190–6195 (2006).

28. Hatch, K., Danilowicz, C., Coljee, V. & Prentiss, M. Demonstration that the shear force required to separate short double-stranded DNA does not increase significantly with sequence length for sequences longer than 25 base pairs. *Phys. Rev. E* **78**, 011920 (2008).

29. Mosayebi, M., Louis, A. A., Doye, J. P. & Ouldridge, T. E. Force-induced rupture of a DNA duplex: from fundamentals to force sensors. *ACS Nano* **9**, 11993–12003 (2015).

30. Zhang, C. et al. The mechanical properties of RNA–DNA hybrid duplex stretched by magnetic tweezers. *Biophys. J.* **116**, 196–204 (2019).

31. Liu, Y. et al. DNA-based nanoparticle tension sensors reveal that T-cell receptors transmit defined pN forces to their antigens for enhanced fidelity. *Proc. Natl Acad. Sci. USA* **113**, 5610–5615 (2016).

32. Ma, R. et al. DNA probes that store mechanical information reveal transient piconewton forces applied by T cells. *Proc. Natl Acad. Sci. USA* **116**, 16949–16954 (2019).

33. Berginski, M. E. & Gomez, S. M. The Focal Adhesion Analysis Server: a web tool for analyzing focal adhesion dynamics. *F1000Res* **2**, 68 (2013).

34. Glazier, R. et al. DNA mechanotechnology reveals that integrin receptors apply pN forces in podosomes on fluid substrates. *Nat. Commun.* **10**, 4507 (2019).

35. Liu, Y. et al. Nanoparticle tension probes patterned at the nanoscale: impact of integrin clustering on force transmission. *Nano Lett.* **14**, 5539–5546 (2014).

36. Swaminathan, V., Fischer, R. S. & Waterman, C. M. The FAK-Arp2/3 interaction promotes leading edge advance and haptosensing by coupling nascent adhesions to lamellipodia actin. *Mol. Biol. Cell* **27**, 1085–1100 (2016).

37. Harris, A. R., Jreij, P. & Fletcher, D. A. Mechanotransduction by the actin cytoskeleton: converting mechanical stimuli into biochemical signals. *Annu. Rev. Biophys.* **47**, 617–631 (2018).

38. Gordon, M. P., Ha, T. & Selvin, P. R. Single-molecule high-resolution imaging with photobleaching. *Proc. Natl Acad. Sci. USA* **101**, 6462–6465 (2004).

39. Basu, R. et al. Cytotoxic T cells use mechanical force to potentiate target cell killing. *Cell* **165**, 100–110 (2016).

40. Wang, J. et al. Profiling the origin, dynamics, and function of traction force in B cell activation. *Sci. Signal.* **11**, eaai9192 (2018).

41. Chen, Y. et al. An integrin $\alpha_{IIb}\beta_3$ intermediate affinity state mediates biomechanical platelet aggregation. *Nat. Mater.* **18**, 760–769 (2019).

42. Zhang, Y. et al. Platelet integrins exhibit anisotropic mechanosensing and harness piconewton forces to mediate platelet aggregation. *Proc. Natl Acad. Sci. USA* **115**, 325–330 (2018).

43. Myers, D. R. et al. Single-platelet nanomechanics measured by high-throughput cytometry. *Nat. Mater.* **16**, 230–235 (2017).

Methods

Synthesis of RSDTPs for cellular experiments. A step-by-step protocol for the synthesis of the DNA tension probe is provided at Nature Protocol Exchange[44]. Briefly, DNA strands I′, II and III were custom-synthesized and purified by Sangon Biotech. Strand I′ was modified with the C6-SH and CH-CH groups at its 5′-end and internal position, respectively. Strand II was modified with a phosphate group at its 5′-end, and the 3′-end of strand III was modified with a BHQ2 quencher. The RSDTP can be synthesized using a three-step procedure (Extended Data Fig. 1b).

Step 1 (synthesis of DNA strand I). First, the disulfide modified strand I′ was treated with 10 mM Tris (2-carboxyethyl) phosphine hydrochloride (TCEP) for 2 h at room temperature to reduce the disulfide bond. After reduction, strand I′ was purified using size-exclusion chromatography (Micro Bio-Spin Size; Bio-Rad), and its concentration was determined using Nanodrop (Thermo Fisher Scientific). Subsequently, strand I′ was labelled with a Cy3B fluorophore by mixing Cy3B maleimide (GE Healthcare) and strand I′ at a 10:1 molar ratio in PBS buffer solution (pH 7.2). The reaction was incubated at room temperature overnight. Then, the product was purified using size-exclusion chromatography and reverse-phase chromatography HPLC (flow rate 1 ml min⁻¹; solvent A: 90% ultrapure water, 10% TEAA; solvent B: 100% acetonitrile, initial condition 10% B for 5 min, then increase the acetonitrile phase by 1% gradient per min) in sequence. To achieve DNA strand I, the Cy3B-labelled strand I′ was conjugated with a cyclic peptide RGDfK-N3 via Cu-catalysed Click chemistry and purified using size-exclusion chromatography. Usually, we did not carry out further purification of the final product (strand I) due to the high reaction yield of the Click chemistry step. Alternatively, the final product can be further purified by denaturing polyacrylamide gel (10%) electrophoresis.

Step 2 (synthesis of DNA hairpin). Strand I, strand II and their complementary template strands were mixed in PBS at a molar ratio of 1.1:1.1:1, and the mixture was then heated up to 95 °C for 4 min and annealed by cooling to room temperature. The two strands (I and II) were then ligated together using DNA ligase (Sangon Biotech). The mixture was separated by 10% denaturing polyacrylamide gel electrophoresis. The desired band was cut from the gel, and then minced and placed in a PBS solution for at least 10 h at 4 °C to extract the DNA product. After two extractions, the product was purified using a 0.2-μm centrifuge tube filter and size-exclusion chromatography.

Step 3 (achieving the final RSDTP). The DNA hairpin and strand III were mixed in PBS solution (pH 7.2) at a molar ratio of 1:1.1 in an Eppendorf tube. The mixture was first denatured at 95 °C for 5 min and then allowed to cool to room temperature. The DNA probe was then formed to their secondary structure and ready to use.

Synthesis of 56-pN TGT probes conjugated with cRGDfK. The sequences and modifications of the single-stranded DNAs (ssDNAs) used in the synthesis of TGTs (56 pN) are shown below:

5′-CAC AGC ACG GAG GCA CGA CAC /SH-C6/-3′.
Complementary ssDNA is 5′-GTG TCG TGC CTC CGT GCT GTG-/Biotin/-3′.

Cyclic peptide RGDfK was conjugated to the sulfhydryl-modified ssDNA through the heterobifunctional crosslinker Sulfo-SMCC (Thermo Fisher Scientific), which contains a N-hydroxysuccinimide (NHS) ester and maleimide group that allows reaction with the thiol group on the thiol-modified DNA and amine on cRGDfK. Conjugation of cRGDf) with Sulfo-SMCC was performed in PBS (pH 7.2) and the product of cRGDfK–maleimide was separated using reverse-phase HPLC. The protocol for cRGDfK–ssDNA conjugation was shown as follows: (1) the disulfide bonds between the thiol-modified ssDNAs were reduced with 10 mM TCEP in PBS (100 mM sodium phosphate,150 mM sodium chloride, pH 7.2). Size-exclusion chromatography (Micro Bio-Spin Size; Bio-Rad) was used to separate ssDNAs from other small molecules. (2) The conjugation of cRGDfK–maleimide with thiol-DNA was performed in PBS (100 mM sodium phosphate, 150 mM sodium chloride, 1 mM EDTA, pH 7.2) and the product of cRGDfK-modified DNA was separated and purified by denaturing polyacrylamide gel (20%) electrophoresis. RGD-DNA and biotin-DNA were annealed in PBS before incubation on PEG-biotin coverslips.

For TGTs that were immobilized on glass through an Au-S bond, the sequences and modifications are shown below:

Ligand strand: 5′-/CHCH/TGAGAGCACGGTGGCACGAGAG-3′.
Disulfide strand: 5′-/Disulfide C6/
TTTTTTTTTTCTCTCGTGCCACCGTGCTCTC-3′.
Ligand strand was modified with a cRGDfK via Cu-catalysed Click chemistry.

Synthesis of RSDTPs for SMMT experiments. All force probes used for the magnetic tweezer experiments were custom-synthesized and purified by Sangon Biotech, and the sequences are shown in Extended Data Fig. 2a. The sequences of the 17-pN and 45-pN probes are identical to the RSDTPs used in the cell experiments. To better identify the unfolding event of the 56-pN probe in the EFC experiment, an additional fragment was added to extend the length of the entire sequence. Furthermore, all the sensor domains were ligated with a long biotin modified handle on its 3′-end through cohesive ends (5′GCCG3′) using T4 DNA ligase.

Magnetic tweezers set-up. Our home-built magnetic tweezer apparatus is implemented on an inverted microscope (Olympus, IX 73) as previously described[30]. The magnetic field is generated by a pair of vertically aligned permanent magnets (with a 1-mm gap) placed above the flow cell, from which the vertical position and rotation are controlled by a translation stage (PI, P-725.CD1) and a stepper motor (PI, M126.PD1), respectively. The light-emitting diode (623 nm, 5 mW, home-made) emits a collimated light that illuminates the magnetic beads in a flow cell through the gap between the magnets. The images were captured by a ×100 oil-immersion objective (Olympus, UPlanSApo NA 1.40) and an sCMOS camera (Daheng, MER-230-168U3, 640 × 480 pixels, 200 Hz). Software written in LabView (National Instruments) was used to record images and real-time track the three-dimensional position of the beads at 200 Hz.

EFC measurements. We employed a similar procedure to create the bead–DNA tethers in a flow cell for EFC measurements as previously reported[30]. Briefly, the flow cell consists of two coverslips separated by a double layer of Parafilm. First, non-magnetic polystyrene beads (3 mm in diameter) were nonspecifically adsorbed on the top surface of the bottom coverslip to act as reference beads. Then, the coverslip was functionalized with a layer of streptavidin to immobilize biotinylated DNA probes. Subsequently, the magnetic beads functionalized with biotin (Thermo Fisher, M270) were added into the flow cell to link the DNA probes. To measure the extension of a given DNA probe, we used the permanent magnets to apply a pulling force to the magnetic beads at a load rate of 1pN s⁻¹ and simultaneously tracked the DNA-tethered bead and a reference bead at a frequency of 200 Hz. To reduce the effects of thermal drift, we measured the extension of the magnetic bead with respect to the extension of the reference bead as the extension of DNA-hairpin unfolding. Magnetic forces were directly evaluated by Brownian motion analysis. All measurements were carried out at 22 °C in PBS. The rupture force of the DNA probe was defined as the value of the force at each unfolding event in each EFC.

Estimation of rupture force of RSDTP. While the RSDTP is in unzipping configuration, we applied the method as described by Woodside et al.[27] to calculate the $F_{1/2}$ at which the closed and open states of the hairpin probe are equally populated. The free-energy landscape for nucleic acid hairpins is given as follows:

$$\Delta G(F, \Delta x) = \Delta G_{\text{fold}} + \Delta G_{\text{stretch}} + F\Delta x$$

Where ΔG_{fold} is the free energy of unfolding the DNA hairpin at zero force and estimated from nearest-neighbour energy parameters by using IDT OligoAnalyzer 3.1 (ΔG_{fold}). F is the externally applied force, Δx is the displacement of the two ends of hairpin, $\Delta G_{\text{stretch}}(x)$ is the free energy for stretching the unfolded ssDNA from $F=0$ to $F=F_{1/2}$, which is estimated by using a worm-like chain model as follows:

$$\Delta G_{\text{stretch}}(x) = \frac{k_B T}{L_P} \frac{L_0}{4\left(1 - \frac{x}{L_0}\right)} \left[3\left(\frac{x}{L_0}\right)^2 - 2\left(\frac{x}{L_0}\right)^3 \right]$$

Here, k_B is the Boltzmann constant, L_p is the persistence length of the ssDNA (1.3 nm), L_0 is the contour length of the ssDNA (0.63 nm per nucleotide), x is the hairpin extension from equilibrium calculated as (0.44 n) nm, where n is the nucleotide number of the hairpin, and 0.44 nm is an approximate extension per nucleotide produced by stretching force, and T is the temperature.

When $F=F_{1/2}$, $\Delta G(F, \Delta x)=0$, thus, $F_{1/2}$ can be calculated as follows:

$$F_{1/2} = \frac{\Delta G\, \text{fold} + \Delta G\, \text{stretch}}{\Delta x}$$

Here, Δx was estimated as $(0.44 \times n - 2)$ nm after taking into account the initial helix width of 2 nm.

While the RSDTP is in shear configuration, the critical rupture force f_c was defined as the magnitude of force that was sufficient to cause 50% of the duplexes to rupture within an observation time. There have been several methods developed to predict the f_c for duplex disruption under the shear mode[23,28]. Here, we chose the equation described by Mosayebi et al.[33] as follows:

$$f_c = \frac{\Delta G_{\text{bp}}}{N\delta - \delta_0} - \frac{\Delta G_{\text{obs}} + \Delta G_0}{N\delta - \delta_0}$$

Here, N is the number of base pairs under shearing. ΔG_{bp} is the free-energy cost of one base-pair disruption. δ is the increased extension per base pair of the transition state relative to the duplex. ΔG_{obs} is the free-energy barrier that must be surmounted before reaching the transition state from the fully duplex when $f=0$. For simplicity, we assume that the transition state is a single base-pair state; hence, $\delta = \delta_0$, and $\Delta G_{\text{bp}} = \Delta G_0$. $\Delta G_{\text{bp}} = 1.5$ kcal mol⁻¹, $\delta = 0.15$ nm (ref. [33]). Given that the DNA-hairpin structure is more stable than the DNA-duplex structure, we set the $\Delta G_{\text{obs}}/\Delta G_{\text{bp}} = 3\sim4$ for the unfolding force estimation of RSDTP.

For simplification, we also treated the 45-pN RSDTP as a pure shearing mode. Although the accuracy of this treatment may be slightly lower than the computer-simulation results[33], the range of estimated values still agrees well with our experimental values.

Synthesis of AU NPs. The synthesis of 5-nm citrate-stabilized Au NPs was primarily based on the method described by Puntes et al.[45]. Briefly, to synthesize 3.5-nm Au NPs as a seed, 1 ml of $HAuCl_4$ (25 mM) was injected into a reaction solution containing 150 ml of sodium citrate (2.2 mM), 0.1 ml of tannic acid (2.5 mM) and 1 ml of potassium carbonate (K_2CO_3, 150 mM) at 70 °C. The reaction was completed in 5 min. To further grow these seeds, the solution was diluted (1:3) by extracting 55 ml of the sample and adding 55 ml of sodium citrate 2.2 mM. When the temperature reached 70 °C again, two subsequent injections of 0.5 ml of $HAuCl_4$ (25 mM) were added at an interval of 10 min, and 5-nm Au NPs at the concentration of 70 nM was achieved after about 10 min. The extinction spectrum of the Au NPs was measured using a NanoDrop microvolume spectrophotometer (Thermo Fisher), and the size of the Au NPs was measured using a transmission electron microscope.

Surface preparation. The procedures for glass surface functionalization and Au NP immobilization were slightly adapted from methods developed by the Salaita Lab as previously described[31]. Circular coverslips (25 mm in diameter, 130 µm in thickness) were rinsed and sonicated three times in nanopure water (18.2 MΩ cm) and then sonicated in acetone for 20 min. After drying in an oven, the coverslips were activated in oxygen plasma for 10 min (30 s.c.c.m., 200 mttor) to achieve a hydroxylated surface. Subsequently, coverslips were functionalized with amine groups by incubating the coverslips in ethanol with a 1% v/v (3-aminopropyl) triethoxysilane (Sigma-Aldrich) in ethanol for 1 h. The coverslips were then passivated by covering with 200 µl of 0.1 M fresh sodium bicarbonate solution containing 5% w/v mPEG-NHS (MW 2000) and 0.5% (w/v) lipoic acid-PEG-NHS (MW 3400). After incubation at 4 °C overnight, the surface was washed with nanopure water. Then, 10 µl of 14 nM Au solution was added on the coverslip surface and incubated for 30 min at room temperature, followed by three rinses with nanopure water and further sonication of the coverslips for 1 min to remove nonspecific bound Au NPs. The density of the Au NPs on the surface was determined using atomic force microscopy (Bruker, BioScope Resolve). Finally, 50 nM RSDTPs (or a mixed-probe sample containing 4 nM RSDTP and 200 nM TGT) in PBS (10 mM sodium phosphate, 1 M NaCl, pH 7.2) was added onto the surface and incubated at room temperature for 1 h. RSDTP-modified coverslips were rinsed with PBS solution to remove nonspecifically bound probes. These modified coverslips were then assembled into cell imaging chambers (Attofluor, Life Technologies) and immediately used for cell experiments.

Image acquisition and analysis. All images and videos were acquired using a Nikon Eclipse Ti2 inverted microscope with Nikon LU-N4 laser units equipped with four lasers (405 nm, 488 nm, 561 nm and 640 nm) (15 mW), an autofocus system, a ×100 oil objective (Nikon, 1.49 NA) and an ANDOR EMCCD (1,024 × 1,024 pixels) camera. Images were captured with Nikon NIS-Elements software. A stage top chamber (Okolab) fits in the *x*–*y* stage of the microscope, connects to Okolab temperature, gas and humidity controllers and creates the proper environment (37 °C, 5% CO_2) for live-cell imaging right on the microscope stage. An objective warming apparatus was used to reduce the focus drift caused by the temperature change. RSDTP-modified coverslips were inserted into a cell image chamber (Thermo Fisher) ready for cell seeding. Excitation of GFP, Cy3B and Atto647N was accomplished using 488 nm, 561 nm and 640 nm lasers with a power of 1.5 mW, 1.5 mW and 4.5 mW, respectively. Excitation and emission were filtered through a 405/488/561/647 quadband cube (TRF89902, Chroma), and images were acquired using 200-ms exposure time. Image data were processed with ImageJ and Matlab software.

Cell culture and transfection. NIH-3T3 mouse embryonic fibroblasts were cultured in Dulbecco's modified Eagle's Medium (DMEM) supplemented with 10% cosmic calf serum, HEPES (9.9 mM, Sigma), sodium pyruvate (1 mM), L-glutamine amide (2.1 mM), penicillin G (100 IU ml^{-1}) and streptomycin (100 µg ml^{-1}) and incubated at 37 °C with 5% CO_2. Cells were passaged at 70% confluence and plated at 10% density using standard cell culture procedures. All cell transfections were completed in 24-well plates. All procedures are based on standard protocols provided by Life Technologies. Briefly, 4×10^4 cells were seeded in each well 1 day before transfection. During transfection, 1 µg of DNA was mixed with Lipofectamine LTX and Plus reagent (Invitrogen) for each well and incubated for 24–48 h before imaging.

Materials. Cy3B maleimide was purchased from GE Healthcare Life Science (product code: PA63131) and Atto647N maleimide was purchased from Sigma-Aldrich. All DNA oligonucleotides were custom-synthesized by Sangon

Biotech. Cyclic peptide RGDfK-N3 was custom-synthesized by Shanghai Top-Peptide Biotechnology. APTES was purchased from Sigma-Aldrich. mPEG-NHS (MW 2000) and lipoic acid-PEG-NHS (MW 3400) were purchased from Hua-Teng Pharma. Micro Bio-Spin P-6 gel columns was purchased from Bio-Rad (product code: 7326221). TCEP, ascorbic acid and sodium citrate were purchased from J&K Scientific. The ROCK inhibitor Y-27632 was acquired from Yeasen Biotech and the myosin II ATPases inhibitor blebbistatin was purchased from APExBIO Technology. Unless otherwise noted, all the other reagents were purchased from Sangon Biotech.

Statistics and reproducibility. Unpaired two-sided Student's *t*-test was used to calculate the *P* values when comparing the statistically significant difference between two groups. $P < 0.05$ was considered to be significant. Statistics were performed using GraphPad Prism 8 and Excel. All statistical data were derived from at least three biologically independent experiments, unless otherwise indicated, and the number of samples are stated in the respective figure legends. The exact numbers of independent experimental repeats for representative micrographs are stated in the corresponding figure legends.

Reporting Summary. Further information on research design is available in the Nature Research Reporting Summary linked to this article.

Data availability
The raw image data generated and analysed that support the findings of this study are available from the corresponding author upon reasonable request. Source data are provided with this paper.

Code availability
The behaviour of FAs in cells was analysed using the Focal Adhesion Analysis Server (FAAS): a web tool for analysing FA dynamics (https://faas.bme.unc.edu).

References
44. Li, H., Hu, Y., Sun, F., Chen, W. & Liu, Z. A reversible shearing DNA-based tension probe for cellular force measurement. *Protocol Exchange* https://doi.org/10.21203/rs.3.pex-1451/v1 (2021).
45. Piella, J., Bastús, N. G. & Puntes, V. Size-controlled synthesis of sub-10-nanometer citrate-stabilized gold nanoparticles and related optical properties. *Chem. Mater.* **28**, 1066–1075 (2016).

Acknowledgements

Author contributions
Z.L. and H.L. conceived and initiated the project. H.L. designed and performed all the experiments with the help of Y.H., F.S., P.L., W.C., J.M., W.W., L.W. and P.W. C.Z and X.Z. performed the SMMT experiments. Z.L. supervised the project and wrote the manuscript.

Competing interests
The authors declare no competing interests.

Additional information
Extended data is available for this paper at https://doi.org/10.1038/s41556-021-00691-0.

Supplementary information The online version contains supplementary material available at https://doi.org/10.1038/s41556-021-00691-0.

Correspondence and requests for materials should be addressed to Z.L.

Peer review information *Nature Cell Biology* thanks Khalid Salaita and the other, anonymous, reviewer(s) for their contribution to the peer review of this work.

**Reprints and permissions information** is available at www.nature.com/reprints.
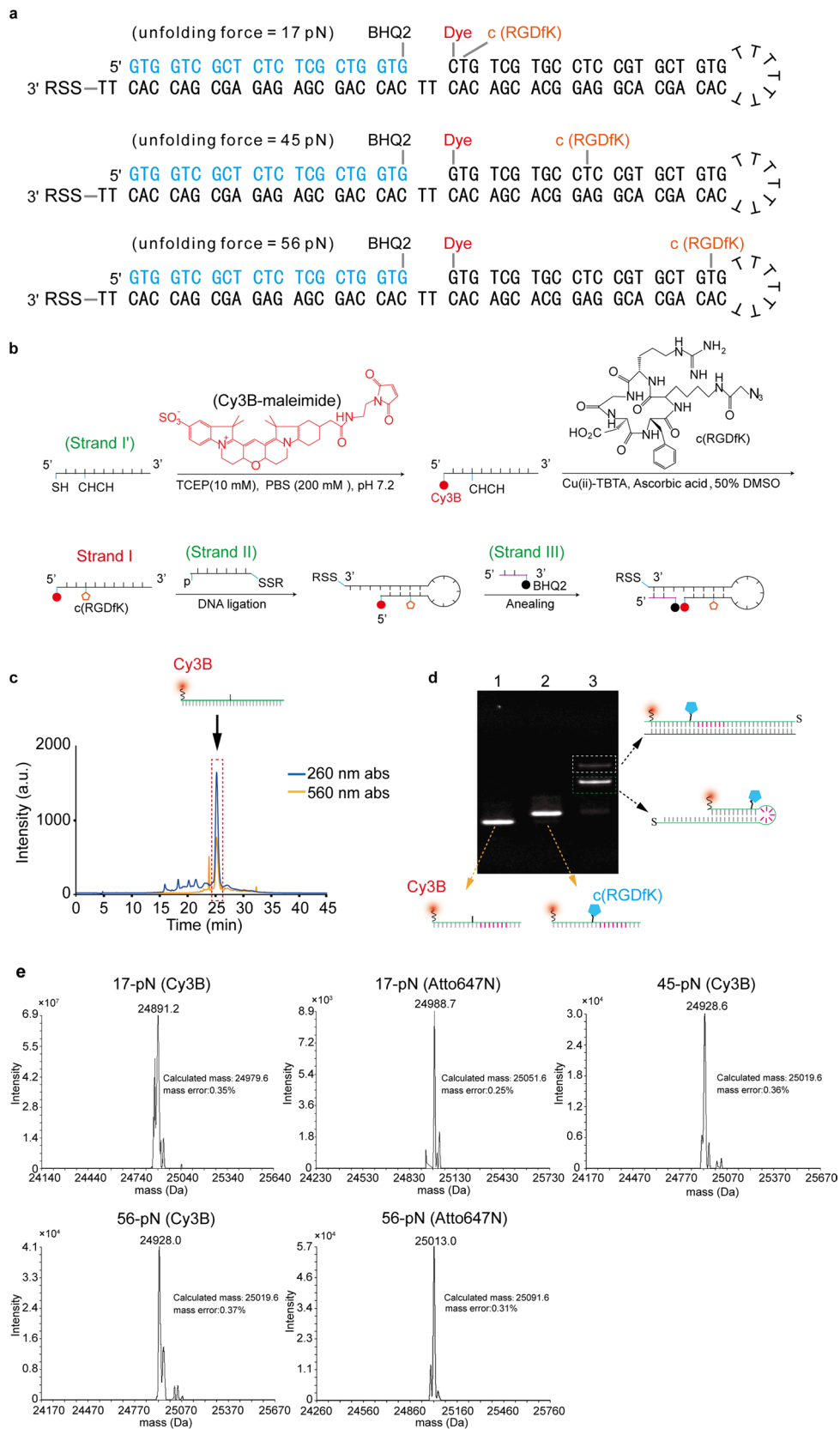
Extended Data Fig. 1 | Synthesis scheme and characterizations of RSDTPs. a, The structures and oligonucleotide sequences of 17-pN, 45-pN and 56-pN RSDTPs. **b**, Detailed chemical schemes for the synthesis of RSDTPs. **c**, Representative HPLC traces of DNA strand I' modified with a Cy3B dye (denoted by dashed rectangle frame.) (**d**) Analysis of assay products by 10% denaturing polyacrylamide gel electrophoresis, lane 1: strand I'-Cy3B; lane 2: strand I'-Cy3B-c(RGDfK); lane 3: extra-long single-stranded DNA (elssDNA, highlighted by a black arrow). Note that, the weaker band above is a complex formed by a small amount of elssDNA and the template strand. The image is the representative of at least three independent biological replicates. **e**, Representative electrospray ionization mass spectrums of elssDNA.
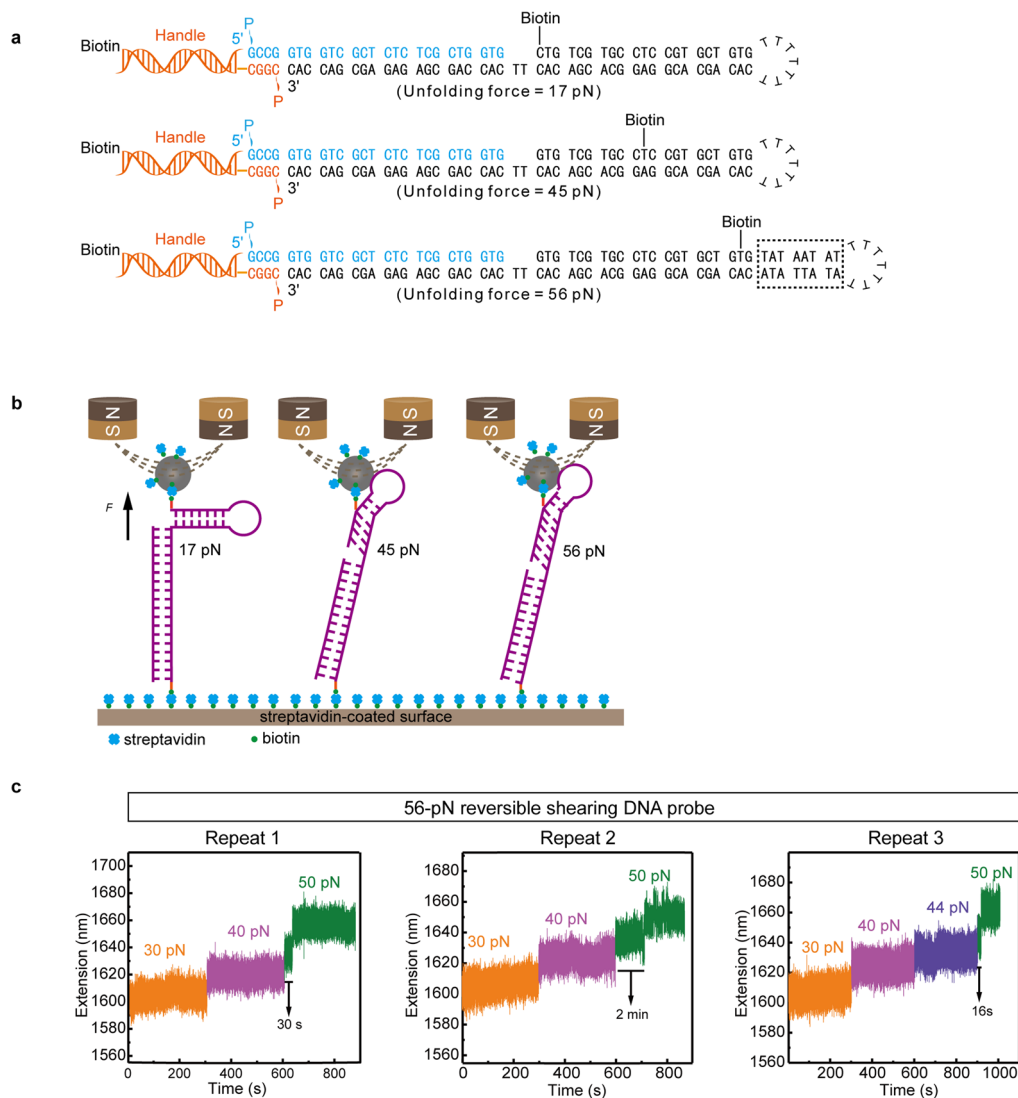
Extended Data Fig. 2 | Schematic diagrams of the composition of the hairpin tension probes for calibration and experimental method of single molecule magnetic tweezer experiments. a, The geometries and compositions of the force probes used for calibration. All probes, combined with a complementary strand (blue) at their 3'end, were ligated to the biotin modified dsDNA handle. For the 56-pN probe, the sequence highlighted by a rectangular is only used to extend the entire length of probe without significantly affecting the mechanical properties. **b**, Schematic depiction of the single-molecule magnetic tweezer experiments. The probes are immobilized to the streptavidin-coated glass surface through their DNA handles. To unfold the probe, pulling forces were applied to a streptavidin-coated magnetic bead by permanent magnets. **c**, Mechanical stability measurements for 56-pN reversible shearing DNA probe. The results show that the 56-pN probe does not unfold even if probe was exposed to a lower level of forces (30–44 pN) for more than 10 minutes, and the unfolding event is only observed when applied force increases above 50 pN and lasted for more than ten seconds.
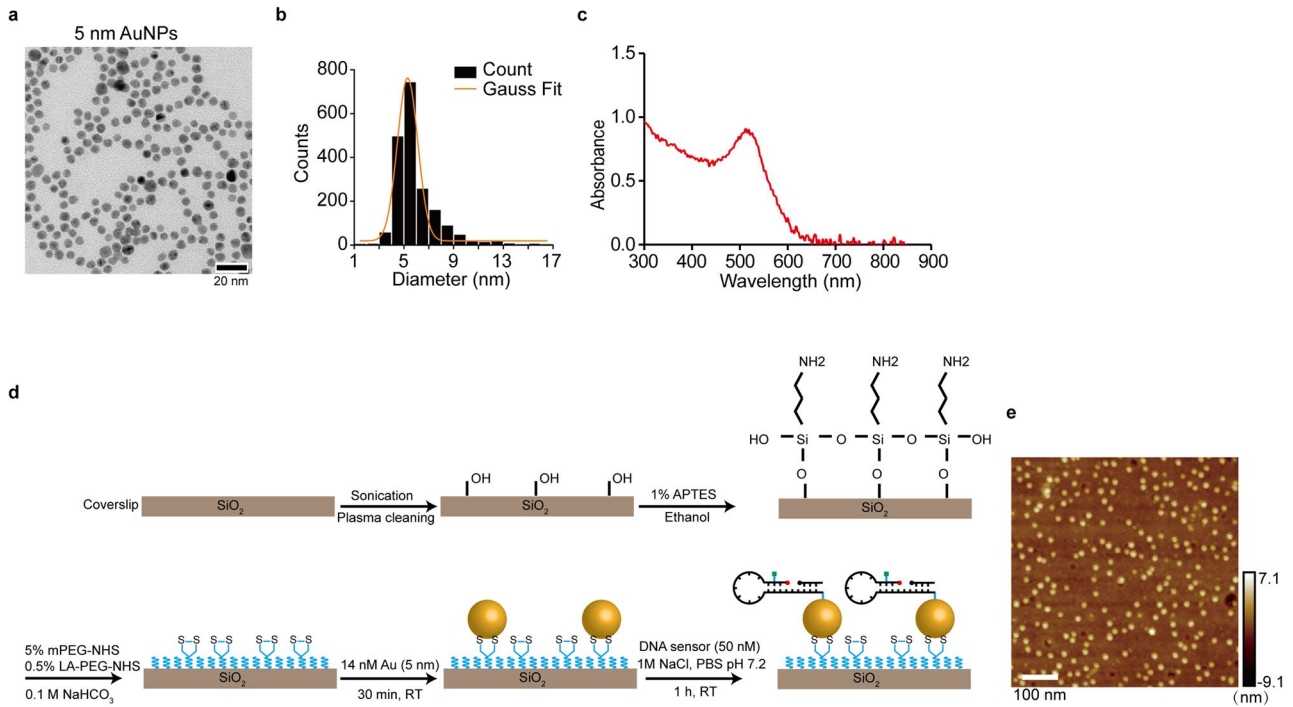
Extended Data Fig. 3 | Characterization of AuNPs and RSDTPs functionalized surfaces preparation. a-b, Representative TEM images of AuNPs (**a**) and corresponding size distribution profiles (**b**). **c**, UV-VIS spectra of 5 nm AuNPs. **d**, Stepwise procedures for preparing RSDTPs functionalized surfaces (see online methods). **e**, The representative AFM image showing the spatial distribution of the AuNPs immobilized on a glass coverslip.
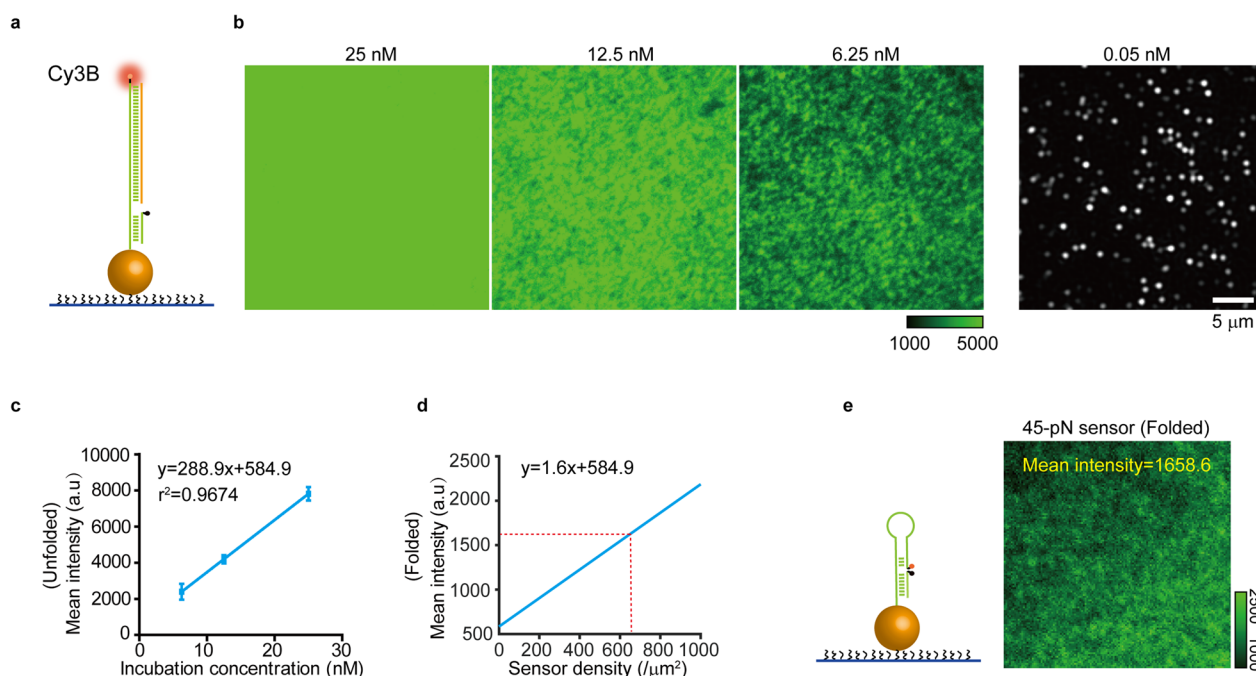
Extended Data Fig. 4 | Determination of DNA probe density on Au nanoparticles surface. To calibrate the surface density of the DNA tension sensor, we used the method described by Wang and Ha et al.[23] to plot the relationship between the fluorescence grayscale units of the sample (mean intensity) and the DNA probe density. First, we incubated aqueous solutions containing 25 nM, 12.5 nM, and 6.25 nM Cy3B-unfolded DNA probe (a scrambled DNA hairpin probe annealing with a complementary strand, the structure was shown in **a**) on the AuNPs-modified coverslips for 30 minutes, then washed off the unbinding probes and measured the average fluorescence intensity of glass as a function of the incubation concertation of the Cy3B-unfolded DNA probe (**b**). There is a linear relationship between the mean fluorescence intensity of the surface and the DNA incubation concentration within this concentration range (**c**). By extrapolation, incubation of 0.05 nM Cy3B-unfolded DNA probe on the surface should correspond to mean fluorescence intensity of 14.4. we also found a molecular density of 0.149 molecules/μm^2 on the surface (0.05 nM) using a single-molecule TIRF image (**b**). Taken together, 96.6 units in mean fluorescence intensity on the Cy3B-unfolded DNA probe surface is equivalent to 1 molecule/ μm^2. Given that the average QE of the Cy3B-folded DNA probe is 98.3% (Fig. 1 in main text), the 1.6 units mean fluorescence intensity on the RSDTP-Cy3B coated surface should be equivalent to 1 molecule/ μm^2. We could also plot a calibration curve between intensity and molecular density for RSDTP (Cy3B) coated surface, as shown in **d**. This calibration curve allows us to determine RSDTP (Cy3B) surface density by measuring the average intensity of a coverslip. For example, the 45-pN RSDTP coated surface's molecular density was estimated to be 671 molecules/μm^2 (**e**).
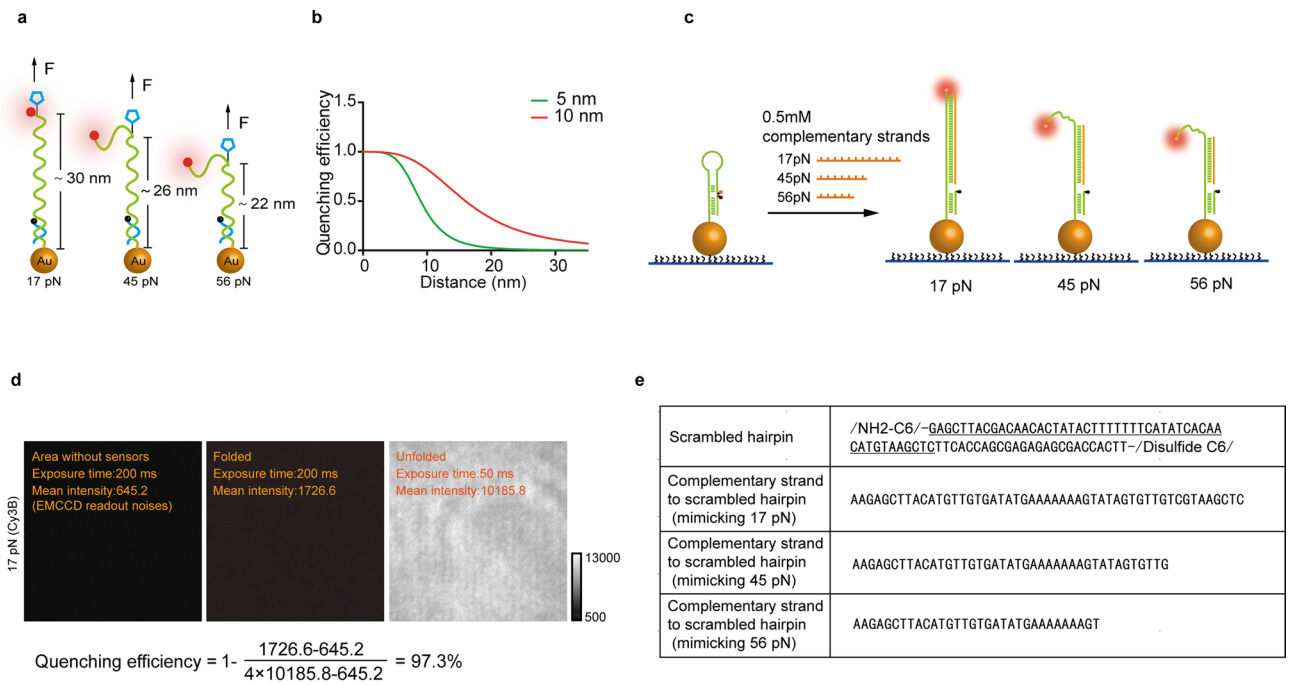
Extended Data Fig. 5 | Determination of fluorescence quenching efficiency (QE) of RSDTPs on a coverslip. a, Estimate the distance between the AuNP surface and fluorophores on mechanically unfolding RSDTPs with different rupture forces by assuming a contour length of 0.44 nm per nt. **b,** Plots of the quenching efficiency as a function of distance from fluorophore to AuNPs with diameters of 5 nm and 10 nm based on the NSET model (Supplementary Note 2). The quenching efficiency (QE)-distance simulation results suggested that the effect of 5 nm AuNP on the Cy3B fluorophore beyond a distance of 20 nm is negligible. **c,** Schematic diagram of measuring the fluorescence quenching efficiency of RSDTPs on a solid surface. To mimic the folded and unfolded states of different RSDTPs, we hybridize complementary DNA strands (preheated to 95 °C) with different length to a scrambled hairpin probe (sequences shown in **e**). The QE values are calculated by measuring the fluorescence intensities before and after the addition of complementary strands. **d,** An example of QE measurement. The QE value of 17-pN RSDTP was calculated as 97.3% by measuring the readout noise of EMCCD, surface fluorescence intensities before and after addition of complementary strands. **e,** Table listing the sequences of the DNA used in this assay.
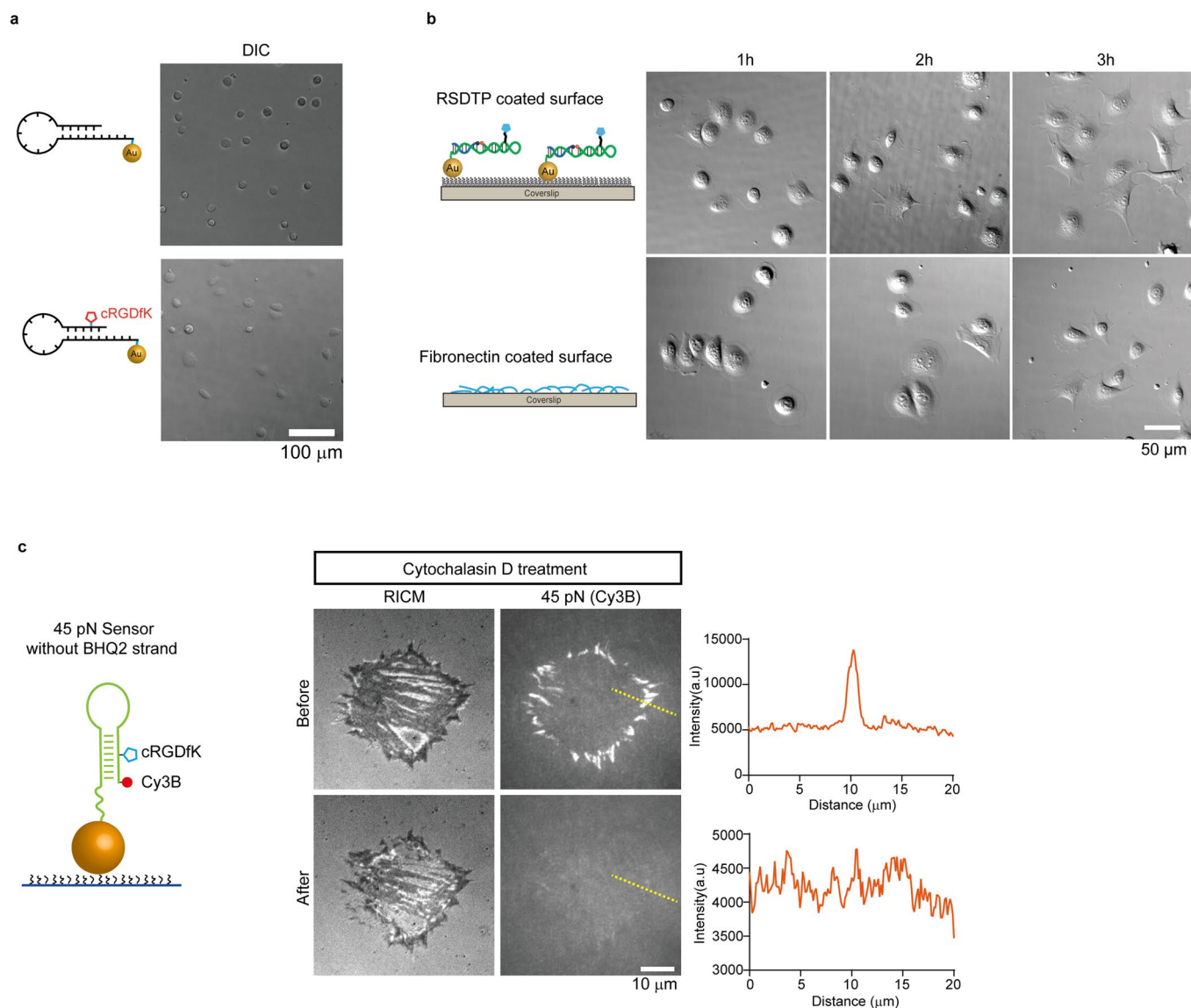
Extended Data Fig. 6 | Control experiments confirmed the reliability and reversibility of the tension probes. a, Comparison of DIC images for cells plated on sensors with and without RGD peptide. No cell attachment was found on surface coated with sensors lacking RGD peptide, suggesting that tension signal is specially generated through RGD-integrin interactions. **b**, Representative DIC images of NIH 3T3 cells seeded on tension probes and fibronectin-coated coverslips at different time points. **c**, A 45-pN RSDTP that lacks the quencher oligonucleotide was used to further validate the stability and reversibility of tension probes. The images show that the fluorescent background of the surface that lacks the quencher oligonucleotide is three times higher than a surface with the quencher strand DNA. Despite the high fluorescence background of these surfaces, we can still detect a tension signal during cell spreading on these surfaces, because Au NP plays a second quencher here. After treating cells with Cyto D, we found that the tension signals disappeared immediately and didn't leave any dark features, which are often used to determine the stability of tension probes on the surface[18]. The fluorescence profiles along the yellow lines in the images are also shown in the right panel.
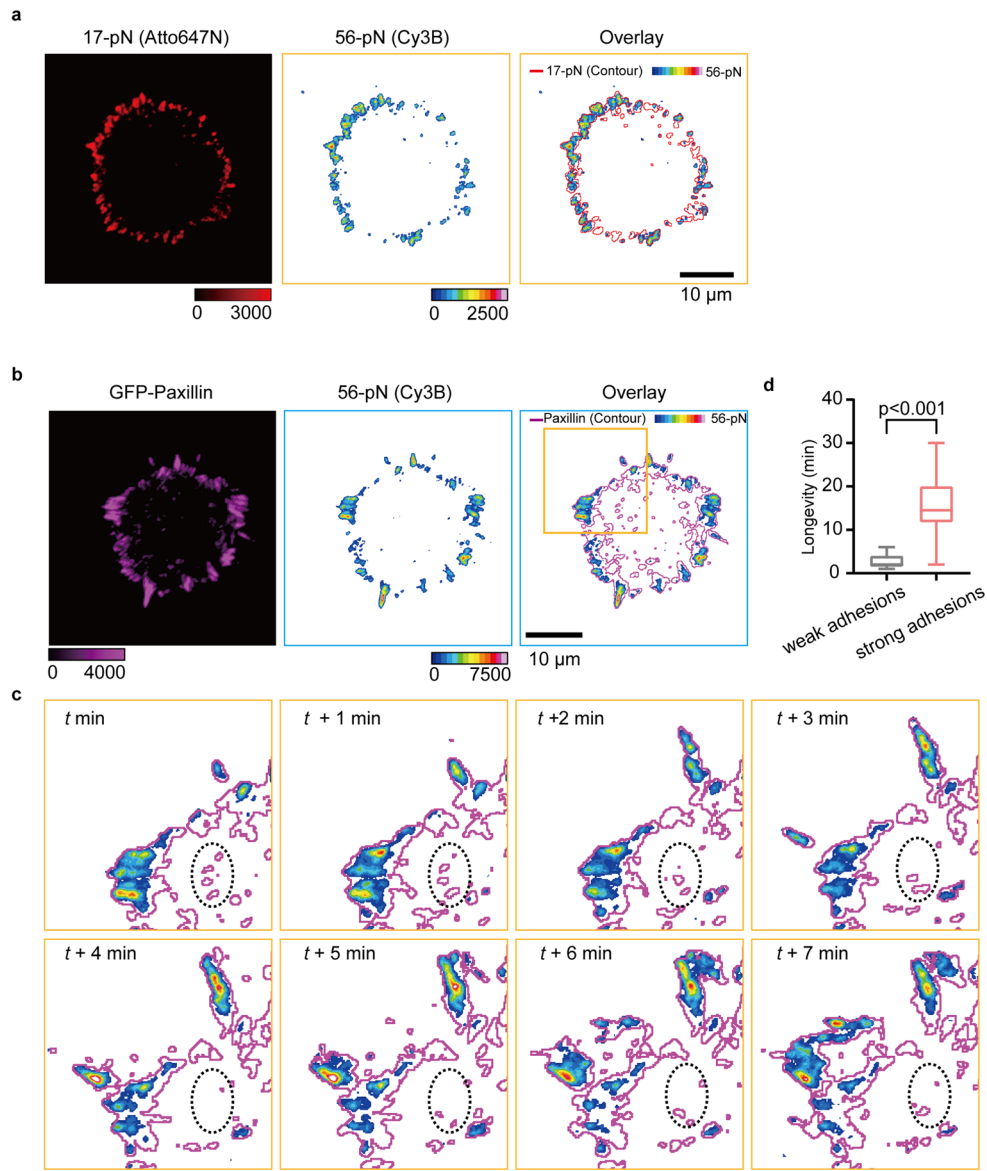
Extended Data Fig. 7 | Further confirmation of the force gradient within FA and the relationship between FA longevity and mechanically hotspots.
**a**, Representative 17-pN (Atto647N), 56-pN (Cy3B) and the overlay tension images for a single NIH/3T3 cells chosen from 2 independent replicates spreading on a coverslip encoded with multiplexed RSDTPs. **b**, Representative 56-pN tension image along with GFP-paxillin of a 3T3 cell chosen from 4 independent replicates. Contour of GFP-paxillin was overlaid with tension signal. **c**, Zoomed-in time-lapse images from yellow-boxed region in **b** showing adhesion structures bearing weak forces undergo a rapid disassembly process. **d**, Longevity of weak and strong adhesions. The box represents 25th and 75th percentiles, the median is denoted by the middle horizontal line with mean value is labeled above each box and whiskers represent 1.5-fold the interquartile range. n = 49 for weak adhesions (structures without 56-pN signal) and n = 34 for strong adhesions (structures contain 56-pN signal) in the cell from **b**. Two-tailed, Student's t-test was used to measure statistical significance, and P-values are shown on the graph.
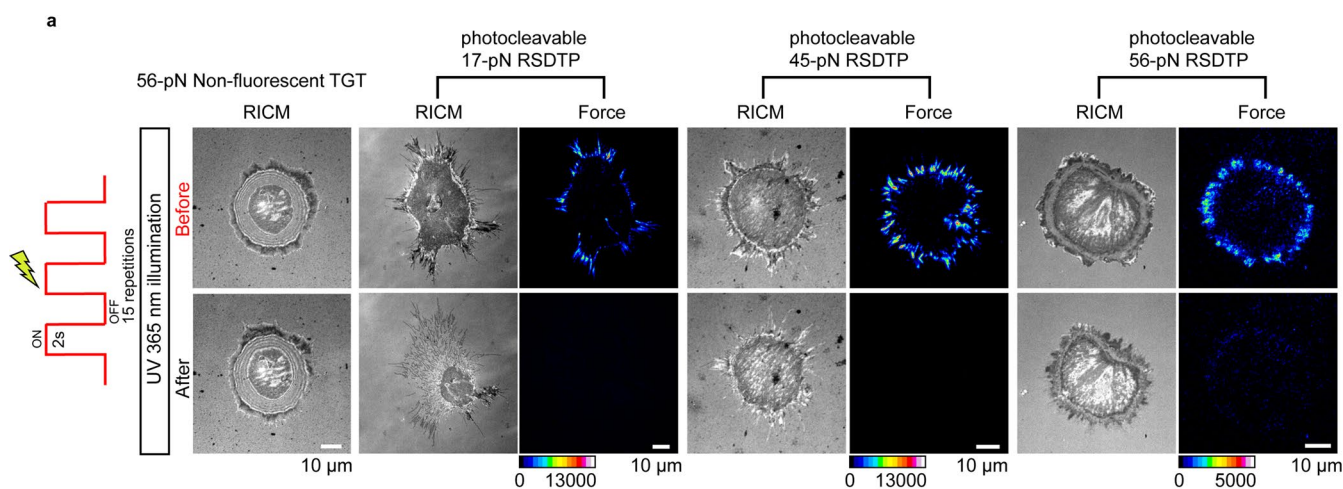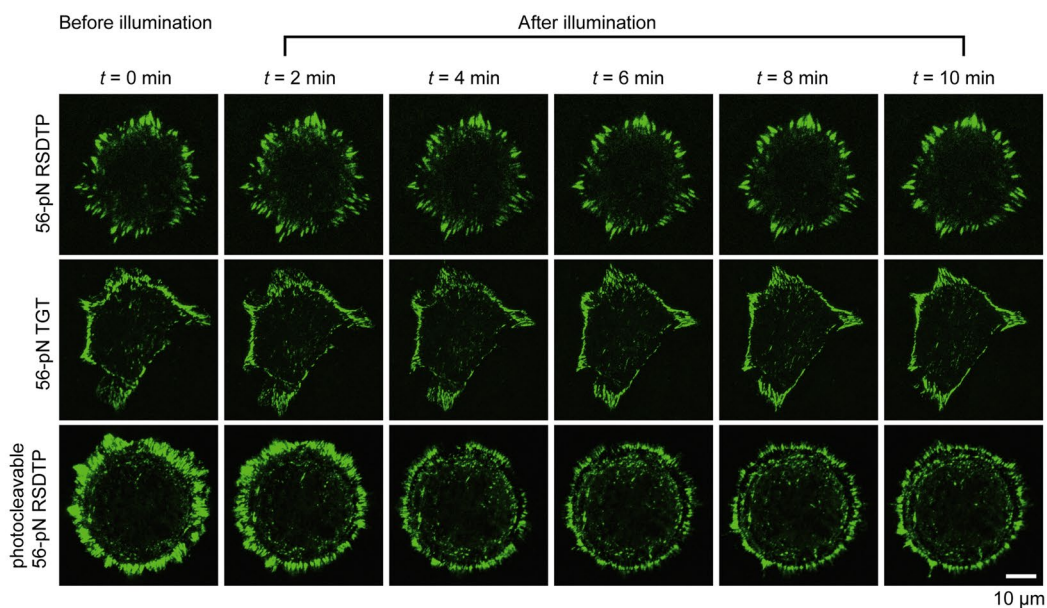
Extended Data Fig. 8 | Testing the reliability of photocleavable RSDTPs. a, Representative RICM and tension images before and after UV illumination (time=30 s, UV-light is operating with a periodic illumination, power density=1.3×10^{-4} μW/μm^2) for cells seeding on different photocleavable RSDTPs coated surfaces. After cleavage of the loop of probes, the cell exhibited a rapid contraction on 17-pN photocleavable RSDTP and slow contraction on 56-pN photocleavable RSDTP, suggested that the RSDTP have been switched to a TGT-like probe. The images were representative of at least 2 independent replicates. **b**, FA dynamics of GFP-Paxillin expressing 3T3 cells seeded on 56-pN RSDTP, 56-pN TGT and 56-pN photocleavable RSDTP coated surface in response to UV illumination. Same illumination condition as in **a** were used here. No significant effect on cells seeded on 56-pN RSDTPs and 56-pN TGT probe coated surfaces were observed. The images were representative of at least 3 independent replicates.
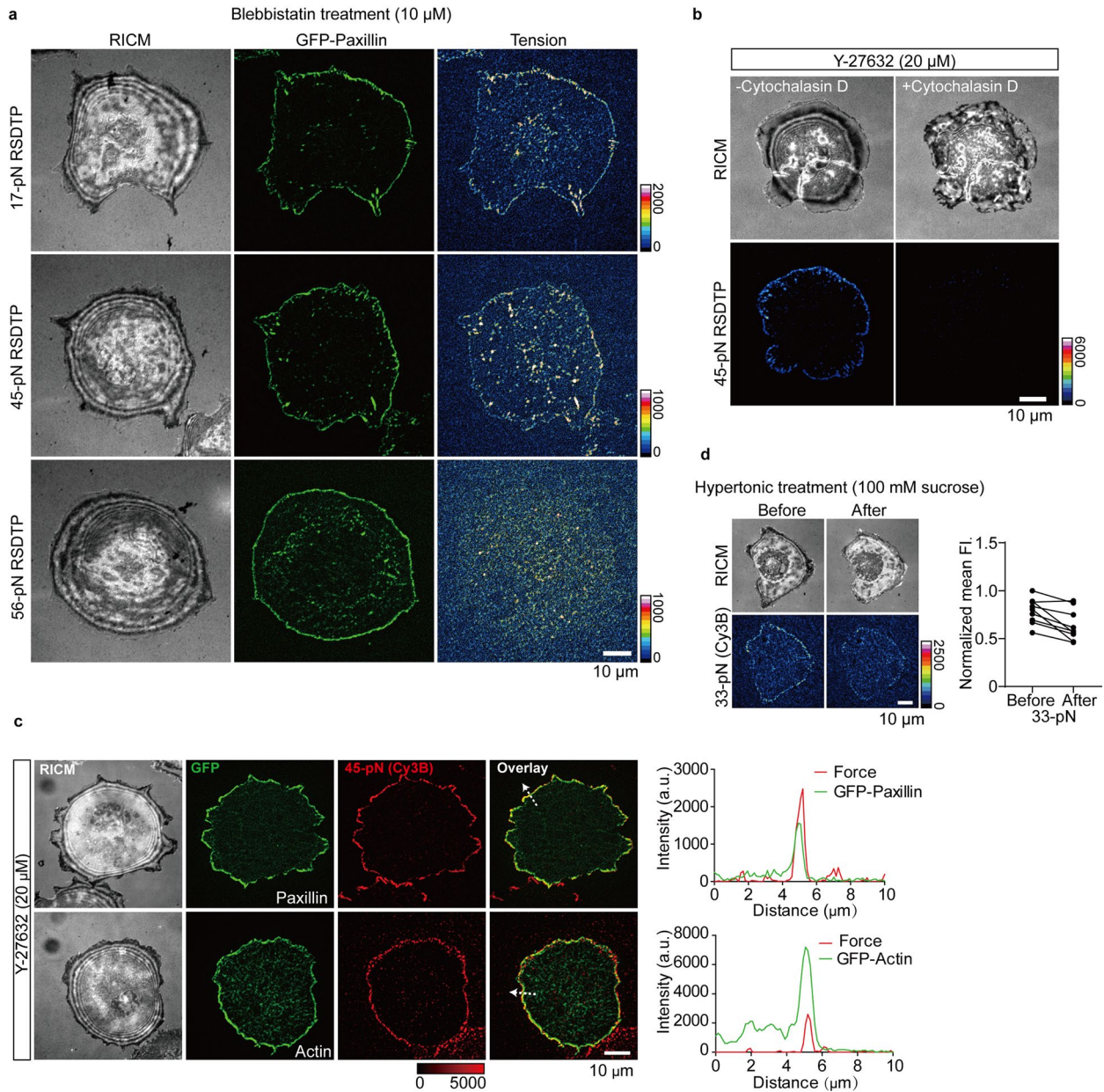
Extended Data Fig. 9 | Images of myosin-independent integrin force. a, Tension images of blebbistatin pre-treated cells adhering to RSDTPs with different rupture forces. NIH 3T3 cells were pretreated with 10 µM blebbistatin for 30 minutes and then seeded on the coverslips. The images were representative of 3 independent replicates. **b**, Representative 45-pN tension images of a Y-27632 pretreated NIH 3T3 cell chosen from 2 independent replicates before and after adding Cytochalasin D. **c**, Co-localization of the integrin tension signal with GFP-Paxillin and GFP-Actin in 3T3 cells treated with Y27632 on 45-pN RSDTP coated surface. Images of RICM (gray), GFP (green), tension (red) and overlay channels were shown. Line scan analysis plot of the region highlighted with dashed white arrows in the overlay images shows the co-localization of the tension with GFP-paxillin and GFP-actin. The images were representative of 3 independent replicates. **d**, Representative 33-pN tension images of a Y-27632 pretreated NIH 3T3 cell chosen from 3 independent biological replicates before and after adding 100 mM sucrose. The right panel shows the change of the thin edge tension signal before and after hypertonic treatment, n=9 cells.
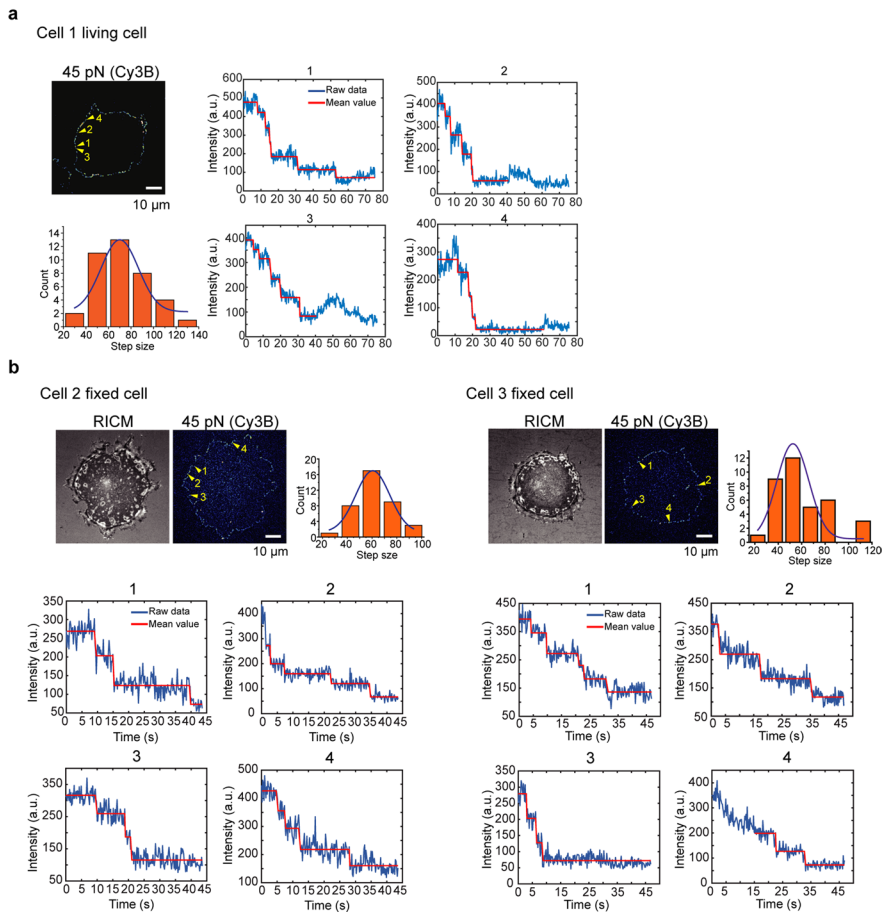
Extended Data Fig. 10 | Single-molecule subunit counting of the force-bearing integrins at thin edges of Y27632 pretreated NIH 3T3 cells. a, Left, a representative tension image (45-pN RSDTP) of a single living cell treated with Y27632 showing punctate fluorescent points. Right, representative intensity traces, under continuous excitation sufficient to cause bleaching of the fluorophores, from four clusters denoted by yellow arrows in the tension image. Below, histogram and gaussian fit of fluorescence intensities for the bleaching steps in the traces (n = 39 steps from cell 1). **b**, Additional data were performed on two fixed cells, and similar results were obtained. (n = 38 steps for cell 2; n = 36 steps for cell 3).

Corresponding author(s):   Zheng Liu

Last updated by author(s):   Mar 29, 2021

Reporting Summary

Nature Research wishes to improve the reproducibility of the work that we publish. This form provides structure for consistency and transparency in reporting. For further information on Nature Research policies, see Authors & Referees and the Editorial Policy Checklist.

Statistics

For all statistical analyses, confirm that the following items are present in the figure legend, table legend, main text, or Methods section.

n/a	Confirmed	
☐	☒	The exact sample size (n) for each experimental group/condition, given as a discrete number and unit of measurement
☐	☒	A statement on whether measurements were taken from distinct samples or whether the same sample was measured repeatedly
☐	☒	The statistical test(s) used AND whether they are one- or two-sided *Only common tests should be described solely by name; describe more complex techniques in the Methods section.*
☒	☐	A description of all covariates tested
☒	☐	A description of any assumptions or corrections, such as tests of normality and adjustment for multiple comparisons
☐	☒	A full description of the statistical parameters including central tendency (e.g. means) or other basic estimates (e.g. regression coefficient) AND variation (e.g. standard deviation) or associated estimates of uncertainty (e.g. confidence intervals)
☐	☒	For null hypothesis testing, the test statistic (e.g. F, t, r) with confidence intervals, effect sizes, degrees of freedom and P value noted *Give P values as exact values whenever suitable.*
☒	☐	For Bayesian analysis, information on the choice of priors and Markov chain Monte Carlo settings
☒	☐	For hierarchical and complex designs, identification of the appropriate level for tests and full reporting of outcomes
☒	☐	Estimates of effect sizes (e.g. Cohen's d, Pearson's r), indicating how they were calculated

Our web collection on statistics for biologists contains articles on many of the points above.

Software and code

Policy information about availability of computer code

Data collection	All image data was acquired by commercial software, NIS-Elements AR.3.2 (Nikon instruments)
Data analysis	ImageJ 1.52v was used to visualize and quantify the fluorescence intensity; Matlab R2019b was used for co-localization analysis between different channels; Graphpad Prism 8, Excel 2019 were used for statistic analysis; FAAS,The Focal Adhesion Analysis Server: a web tool for analyzing focal adhesion dynamics.

For manuscripts utilizing custom algorithms or software that are central to the research but not yet described in published literature, software must be made available to editors/reviewers. We strongly encourage code deposition in a community repository (e.g. GitHub). See the Nature Research guidelines for submitting code & software for further information.

Data

Policy information about availability of data

All manuscripts must include a data availability statement. This statement should provide the following information, where applicable:

- Accession codes, unique identifiers, or web links for publicly available datasets
- A list of figures that have associated raw data
- A description of any restrictions on data availability

The raw image data generated and analyzed that support the findings of this study are available from the corresponding author upon reasonable request. Statistics source data for all figures and supplementary figures are provided with this paper.

Field-specific reporting

Please select the one below that is the best fit for your research. If you are not sure, read the appropriate sections before making your selection.

☒ Life sciences   ☐ Behavioural & social sciences   ☐ Ecological, evolutionary & environmental sciences

For a reference copy of the document with all sections, see nature.com/documents/nr-reporting-summary-flat.pdf

Life sciences study design

All studies must disclose on these points even when the disclosure is negative.

Sample size	Sample sizes calculation were done during cell experiments. For analysis of substructure in cells, e.g., focal adhesion, time-lapse images of 3-5 cells can provide sufficient information on adhesion dynamics (Berginski, M.E. & Gomez, S.M. F1000Res,2013, 2, 68). For measurement of the fluorescence intensity of tension image, more than ten cells were used for analysis for each condition. For calibration of DNA probes, over 45 force-extension curves were used to statistics the average unfolding forces for each type of tension probe.
Data exclusions	No data were excluded from the analysis.
Replication	Attempts at replication were successful. All statistical data were collected from at least 3 independent experiments to verify the reproducibility of the results, unless otherwise noted in the legend.
Randomization	For cell experiments, the same batch of cells were collected for each condition and randomly divided into separate group during an independent experiment, and microscopy images was also randomly selected.
Blinding	No blinding was performed as there were no experimental groups in this study.

Reporting for specific materials, systems and methods

We require information from authors about some types of materials, experimental systems and methods used in many studies. Here, indicate whether each material, system or method listed is relevant to your study. If you are not sure if a list item applies to your research, read the appropriate section before selecting a response.

Materials & experimental systems

n/a	Involved in the study
☒ ☐	Antibodies
☐ ☒	Eukaryotic cell lines
☒ ☐	Palaeontology
☒ ☐	Animals and other organisms
☒ ☐	Human research participants
☒ ☐	Clinical data

Methods

n/a	Involved in the study
☒ ☐	ChIP-seq
☒ ☐	Flow cytometry
☒ ☐	MRI-based neuroimaging

Eukaryotic cell lines

Policy information about cell lines

Cell line source(s)	NIH-3T3 cells were purchased from China Center for Type Culture Collection (CCTCC).
Authentication	Cell lines were not authenticated.
Mycoplasma contamination	The cell lines were not tested for mycoplasma contamination.
Commonly misidentified lines (See ICLAC register)	No commonly misidentified cell lines were used.